Measurements of seismic waves induced by high-velocity impacts: Implications for seismic shaking surrounding impact craters on asteroids

Matsue, Kazuma
Yasui, Minami
Arakawa, Masahiko
Hasegawa, Sunao

(Citation)
Icarus,338:113520

(Issue Date)
2020-03-01

(Resource Type)
journal article

(Version)
Accepted Manuscript

(URL)
https://hdl.handle.net/20.500.14094/90006964

Measurements of seismic waves induced by high-velocity impacts: Implications for seismic shaking surrounding impact craters on asteroids

Kazuma Matsue[1], Minami Yasui[1], Masahiko Arakawa[1], and Sunao Hasegawa[2]

1. Graduate School of Science, Kobe University

1-1, Rokkkodai-cho, Nada-ku, Kobe, Hyogo 657-8501, Japan

2. Japan Aerospace Exploration Agency, Institute of Space and Astronautical Science

3-1-1, Yoshinodai-cho, Chuo-ku, Sagamihara, Kanagawa 252-5210, Japan

Tel: +81-78-803-5741

Fax: +81-78-803-5741

E-mail: minami.yasui@pearl.kobe-u.ac.jp

Manuscript pages: 53

Number of figures: 15

Number of tables: 7

Proposed running head: Impact-induced seismic waves at high-velocity impacts

Corresponding authors:

Minami Yasui

Now at

Graduate School of Science, Kobe University

1-1, Rokkodai-cho, Nada-ku, Kobe, Hyogo 657-8501, Japan

Tel: +81-78-803-5741

Fax: +81-78-803-5741

E-mail: minami.yasui@pearl.kobe-u.ac.jp

Abstract

On asteroids, impact-induced seismic shaking is an important geological process related to the modifications of the surface features that are due to the movement of regolith grains on the asteroid surface. Mass movements caused by seismic shaking (e.g., landslides and crater erasures) were recently observed by several spacecrafts. To elucidate the seismic shaking areas induced by impacts on asteroids, it is necessary to determine the excitation and the decay processes of impact-induced seismic waves. Here we conducted impact cratering experiments using 500-μm quartz sand to simulate an asteroid surface at the Institute of Space and Astronautical Science (ISAS), Japan Aerospace Exploration Agency (JAXA). We used 4.75-mm- and 2-mm-dia. projectiles with density from 14.9 to 1.2 g cm^{-3}; the impact velocity ranged from 7 to 0.2 km s^{-1}. We measured the acceleration waveform by using three to five accelerometers setting on the target surface, and we examined three parameters characterizing the impact-induced seismic wave with varying distances from the impact point: the propagation velocity (V_{prop}), the maximum acceleration (g_{max}), and the half period of the first upward peak (T_{half}). The V_{prop} was obtained to be 52.4 ± 7.2 m s^{-1}, regardless of the impact velocity and the projectile properties, and the T_{half} slightly depended on the impact velocity as ${v_{\mathrm{i}}}^{0.14}$ but was independent of the projectile properties. The g_{max} had a close relationship with the distance from the impact point normalized by the crater rim radius, x/R_{rim}, regardless of the impact velocity and the projectile properties. The obtained empirical equation was

48 shown as $g_{\max} = 10^{2.21}(x/R_{\mathrm{rim}})^{-3.18}$. By using the empirical equations we obtained
49 herein, we observed that the seismic energy normalized by the kinetic energy of a
50 projectile, $E_{\mathrm{s}}/E_{\mathrm{k}}$, decreased with the increase of the normalized distance, x/R_{rim}. We
51 also estimated the area of impact-induced seismic shaking on an idealized small (500 m
52 in diameter) body at the impact velocity of 5 km s^{-1}.
53 **Keywords:** Asteroids; Asteroids, surfaces; Experimental techniques; Cratering; Impact
54 processes

1. Introduction

1.1. Seismic shaking on an asteroid surface

Seismic shaking induced by a high-velocity impact is one of the most important surface geologic processes that occurs on an asteroid surface. Such shaking frequently modifies the asteroid surface topography. Several planetary explorations recently revealed the detailed surface geology of asteroids, and evidence of regolith migration was identified on the asteroid surfaces. For example, NEAR-Shoemaker and Hayabusa spacecrafts obtained numerous close-up images of the asteroids 433 Eros and 25143 Itokawa. The images of the asteroid surfaces showed unconsolidated gravel and pebbles which were typically stacked upon each other [Miyamoto et al., 2007]. Regolith migration was then identified on the asteroid surface as alignments of boulders, landslides, and crater erasures [Veverka et al., 2001; Cheng et al., 2002; Thomas et al., 2002; Robinson et al., 2002; Miyamoto et al., 2007].

These features could be explained by global-scale and/or local-scale seismic shaking caused by high-velocity impacts on the regolith surface. Impact-induced seismic shaking on a global scale could trigger regolith migration under a vacuum and in the microgravitational environment that is typically present on small asteroids [Miyamoto et al., 2007]. These phenomena could preferentially remove small undulations such as small craters.

Asteroid 433 Eros, one of the most intensively studied small extraterrestrial bodies,

was revealed to have surface areas at which the crater number density differed considerably. It also appeared that the number density of small impact craters (<~100 m in diameter) was much smaller than that extrapolated from the >100-m impact craters, based on the cumulative size distribution of impact craters detected on the asteroid [Robinson et al., 2002].

To study this deficiency in the number of small craters, Richardson et al. [2005] developed a theoretical model for the crater erasure process caused by global seismic shaking. They stated that their calculations indicated that the vibration of the regolith layer covering the entire asteroid surface was responsible for erasing the craters. A deficiency in the number of craters with diameters <500 m was observed around Shoemaker crater (within 9 km from the center of the crater), and this unique feature of low crater density suggested that the crater degradation could have been caused by local seismic shaking induced by the formation of Shoemaker crater [Robinson et al., 2002].

Several research groups have carried out numerical simulations to investigate the effect of impact-induced seismic shaking on the motion of particles in the regolith layer of an asteroid surface. Asphaug and Melosh [1993] performed a numerical simulation using a hydrodynamic code for a high-velocity impact, and they examined the seismic resurfacing of the asteroid surface. Greenberg et al. [1994, 1996] proposed a ‘global jolt’ resulting from large impacts on the surfaces of an asteroid such as 243 Ida and 951 Gaspra, and they discussed the effect of the jolt on the crater size distributions. The results of both

95 the Asphaug and Melosh and Greenberg et al. studies suggested that there is a key
96 parameter that induces the resurfacing that is related to impact craters on asteroids, that
97 is, an impact-induced seismic efficiency factor that could be defined by the ratio of the
98 seismic energy to the kinetic energy of the impactor.

99 Such an impact-induced seismic efficiency factor is poorly understood, and only a
100 few impact experiments have been conducted to evaluate impact-induced seismic waves
101 in a laboratory setting. McGarr et al. [1969] conducted high-velocity impact experiments
102 using loose sand and epoxy-bonded sand as the targets and a Lexan projectile at impact
103 velocities of 7–0.8 km s^{-1}. They observed the impact-induced seismic waves by setting
104 accelerometers on the target surface. Their results demonstrated an impact-induced
105 seismic efficiency factor of 6.0×10^{-6} for the loose sand and 7.6×10^{-5} for the bonded
106 sand target.

107 Yasui et al. [2015] conducted impact experiments on targets made of 200-μm-dia.
108 glass beads impacted at the impact velocities of <150 m s^{-1} to study the attenuation rate
109 of the impact-induced seismic wave. They observed that the maximum acceleration, i.e.,
110 $g_{\max}$, of the seismic wave decayed with the distance from the impact point normalized
111 by the crater radius, x/R, according to the following power law equation: $g_{\max} =$
112 $g_0(x/R)^{-2.2}$ within $x/R = 5$. Their calculations revealed that the average impact-
113 induced seismic efficiency factor was 5.7×10^{-5}. However, this result was obtained at
114 impact velocities <150 m s^{-1}, which is much slower than the relative collisional velocities

among asteroids. Moreover, spherical glass beads were used as the target, and these beads might be an idealized granular material simulating asteroid regolith. The seismic efficiency factor had a wide range (10^{-2}–10^{-6}) depending on the impactor and target properties [Gault and Heitowit, 1963; McGarr et al., 1969; Collins et al., 2005] and the impact energies [Shishkin, 2007].

More realistic numerical simulations were recently conducted by using iSALE to reproduce an impact crater formed on cohesive materials such as porous basalt, quartzite, and sandstone. The estimated seismic efficiency factor ranged from 10^{-3} to 10^{-5} for the elastic waves that were induced by the impact at a site far from the impact point [Güldemeister and Wünnemann, 2017; Wójcicka et al., 2019].

We conducted the present study to determine the attenuation rate of a seismic wave propagating through a target simulating an asteroid regolith, and we investigated the impact-induced seismic efficiency factor at high impact velocities (i.e., those comparable to the relative collisional velocities among asteroids). We then carried out impact cratering experiments and measured the impact-induced seismic waves by using accelerometers set on a granular target, following the methods described by McGarr et al. [1996] and Yasui et al. [2015]. For our investigation of the effects of the impact velocity and the projectile properties on the impact-induced seismic waves, the target material (quartz sand) was fixed. We also estimated the impact-induced seismic energy by using a revised sinusoidal wave model delineated by Yasui et al. [2015], and we discuss the

135 impact-induced seismic efficiency factor. We also assessed the seismic shaking area on
136 an idealized small body by using the obtained empirical equations obtained herein and
137 the crater scaling laws.
138
139 *1.2. π-scaling theory*
140 Crater scaling theories are essential to evaluations of planetary-scale impact
141 phenomena under various impact conditions. These theories have been tested in
142 laboratory experiments. In the present study, we applied the π-scaling theory proposed
143 by Holsapple [1993] to our experimental results. This conventional theory for cratering
144 processes can be used to extrapolate our laboratory-scale results to planetary-scale
145 impacts. We used the following non-dimensional scaling parameters, i.e., π_{R}, which is
146 related to the crater radius (R_{c}), and π_2 and π_4, which are related to various impact
147 conditions:

148 $$\pi_{\mathrm{R}} = R_{\mathrm{c}}\left(\frac{\rho_{\mathrm{t}}}{m_{\mathrm{p}}}\right)^{1/3}, \qquad (1)$$

149 $$\pi_2 = \frac{g r_{\mathrm{p}}}{v_{\mathrm{i}}^2}, \qquad (2)$$

150 $$\pi_4 = \frac{\rho_{\mathrm{t}}}{\rho_{\mathrm{p}}}, \qquad (3)$$

151 where ρ_{t} is the bulk density of target, m_{p} is the projectile mass, ρ_{p} is the projectile
152 density, r_{p} is the projectile radius (they are written as $m_{\mathrm{p}} = 4\pi\rho_{\mathrm{p}} r_{\mathrm{p}}^3/3$ for a spherical

153 projectile), g is the gravitational acceleration, and v_i is the impact velocity.

154 In a gravity regime in which the crater formation process is controlled by the gravity
155 of the body, the following relationship is proposed on the basis of a point source
156 approximation and a coupling parameter, $C = r_\mathrm{p} {v_\mathrm{i}}^{\mu} {\rho_\mathrm{p}}^{\nu}$:

157 $$\pi_\mathrm{R} = H_1 \, {\pi_2}^{-\frac{\mu}{2+\mu}} {\pi_4}^{\frac{2+\mu-6\nu}{3(2+\mu)}}, \qquad (4)$$

158 where H_1, μ, and ν are the constants that depend on the target properties, We were able
159 to determine these values in laboratory experiments.

160

161 **2. Experimental methods**

162 *2.1. Impact experiments*

163 We used quartz sand with a mean grain diameter of 500 μm as a target simulating the
164 regolith layer on an asteroid surface. The grains of the quartz sand have irregular shapes
165 but rounded corners. The measured angle of repose was 33 ± 2°, which is much higher
166 than that of the 200-μm spherical glass beads (23 ± 2°) used by Yasui et al. [2015]. The
167 grain density of the quartz sand was 2.7 g cm^{-3} and the calculated bulk density of the
168 quartz-sand target was 1.46 g cm^{-3}; thus, the estimated bulk porosity was approximately
169 42%. The quartz sand was poured into two stainless-steel containers: the larger 60-cm-
170 diameter, 20-cm-deep container was used for the impact velocities >1.1 km s^{-1}, and the
171 smaller 30-cm-diameter, 10-cm-deep container was used for the impact velocities <230

172 m s^{-1}. Before every shots, the surface of the target was flattened with the use of a hard
173 metal ruler.

174 We conducted the impact experiments by using a two-stage vertical gas gun located
175 at the Institute of Space and Astronautical Science (ISAS), Japan Aerospace Exploration
176 Agency (JAXA). Fig. 1a is a schematic of the experimental setup. The 2-m-high target Fig. 1
177 chamber had a 1.5-m diameter and was set below the gun barrel: the chamber was
178 evacuated below 10 Pa before each shot. The impact velocity, v_i, ranged from 6.9 to 1.1
179 km s^{-1}, and we used eight types of projectile with densities ranging from 14.9 to 1.2 g
180 cm^{-3} to study the effects of the projectile density on the crater scaling law and the impact-
181 induced seismic waves.

182 Each of the projectiles was a sphere, made of the following: polycarbonate (PC,
183 density of 1.2 g cm^{-3}), soda-lime glass (Gl, 2.5 g cm^{-3}), aluminum (Al, 2.7 g cm^{-3}),
184 titanium (Ti, 4.6 g cm^{-3}), zirconia (ZrO_2, 5.7 g cm^{-3}), stainless steel (SUS, 7.9 g cm^{-3}),
185 copper (Cu, 9.0 g cm^{-3}), and tungsten carbide (WC, 14.9 g cm^{-3}). The diameter of the PC
186 projectile was 4.75 mm, and the diameter of the other seven projectiles was 2.0 mm. Each
187 projectile was launched in the direction parallel to the gravity acceleration of the Earth,
188 so that it impacted at a direction perpendicular to the target surface.

189 To examine the effects of the grain shape on the cratering process, we also conducted
190 low-velocity cratering experiments using the quartz sand at the impact velocity of 170–
191 227 m s^{-1} in order to compare our results with those of the Yasui et al. [2015] study. It is

192 difficult to achieve an impact velocity below 1.0 km s^{-1} by using the two-stage gas gun
193 at ISAS, and thus our low-velocity cratering experiments were carried out using the same
194 experimental set up as that used by Yasui et al. [2015].
195
196 *2.2. Observations of impact phenomena*
197 We used an uniaxial piezoelectric accelerometer (#SV1113, Nippon Avionics, Tokyo)
198 with a charge amplifier (#AG2101, Nippon Avionics) to measure the acceleration
199 activated on the target surface affected by an impact-induced seismic wave. The charge
200 sensibility was 5.47 pC s^2 m^{-1}, and the response frequency of the acceleration was 0.5
201 Hz–10 kHz. For our investigation of the decay process of impact-induced seismic waves,
202 we set three, four, or five accelerometers (Fig. 1b) on the target surface at 35.3 to 5.1 cm
203 from the impact point, outside of the impact crater rim. The measurement direction of the
204 accelerometers were perpendicular to the target surface; the accelerometers could
205 therefore detect the normal components of the acceleration activated on the surface. The
206 accelerometers were buried at the depth of 2.5 cm (Fig. 1c).
207 Each seismic wave measured by the accelerometers was recorded by a data logger
208 with an A/D conversion rate of 100 kHz (midi LOGGER GL900, Graphtec, Yokohama,
209 Japan). We repeated the cratering experiments using the same impact conditions several
210 times to acquire the seismic wave data at different propagation distances, ensuring that
211 we would have a sufficient amount of data to determine the attenuation rate of the seismic

212 waves.

213 It is necessary to remove any artificial noise added to the actual signals, because such
214 noises are naturally induced by the instantaneous force generated by the projectile
215 launching. This force could activate the vibration of the target container set in the target
216 chamber. The bottom of the target container was thus insulated by a rubber sheet to
217 remove the activated vibration (Fig. 1a) so that the acceleration of each impact-induced
218 seismic wave was measured precisely.

219 We observed the impact phenomena by using a high-speed digital camera (Hyper
220 Vision HPV-X, Shimadzu, Kyoto, Japan) to determine the impact time of each projectile
221 on the target surface. The frame rate was set at 10^5 frames s^{-1}. The impact time could be
222 determined within 10 μs. To synchronize the trigger of the high-speed digital camera with
223 the trigger of the data logger, we generated a trigger signal by using a function generator
224 to send the signal to both devices at the moment when the velocity measurement system
225 detected a signal showing the projectile passing through.

226 After the shot, a photograph was taken just above the target surface for the analysis
227 of the precise distance of each accelerometer from the impact point. We used a digital
228 caliper to measure the rim-to-rim distances in two directions where they were crossed at
229 right angles. The average distance was defined as the rim diameter, D_{rim}. In several shots,
230 we measured a cross-section of the impact crater by using a laser profiler (#LJ–V7300,
231 Keyence, Osaka, Japan) with 10-μm resolution to determine the ratio of the depth to the

232 diameter of the impact crater.

233

234 **3. Results**

235 *3.1. Morphology of impact craters*

236 The experimental conditions and the results on the morphology of the impact craters
237 are summarized in Table 1. Fig. 2 shows the crater profiles obtained under various impact Table 1
238 conditions. As shown in the figure, all of the impact craters formed in these experiments Fig. 2
239 were categorized as a simple crater with a bowl-shaped depression surrounded by a
240 distinct rim. A bright area was spread over the center of the crater floor in each case; this
241 area might have been comminuted quartz sand grains.

242 The impact crater formed by the PC projectile is shown in Fig. 2a, b. The crater size
243 at $v_i = 6.9$ km s^{-1} was about twice that obtained at 1.1 km s^{-1}. When an impact velocity
244 was high (Fig. 2b), several small pieces of black debris were observed on the bright area
245 of the crater floor; these might have been charred broken projectile fragments. Impact
246 craters formed by an Al projectile and a Cu projectile are shown in Fig. 2c, d, and the
247 impact velocity was almost the same: approximately 4 km s^{-1}. The crater size increased
248 with the increase of the projectile density: the crater made by the Cu projectile was 1.3
249 times larger than that by the Al projectile at the density ratio of Cu to Al of approximately
250 3.

251 Fig. 3a is crater profiles obtained with the PC projectiles at different impact velocities. Fig. 3

252 Both the diameter and the depth of the craters clearly became larger as the impact velocity
253 increased. To study the similarity of the crater shapes formed at different impact velocities,
254 we normalized both the vertical and horizontal axes in Fig. 3a by each crater rim radius,
255 R_{rim}, where $R_{\mathrm{rim}} = D_{\mathrm{rim}}/2$, and then we plotted the normalized crater profile at each
256 impact velocity (Fig. 3b). The normalized crater profiles were very similar, regardless of
257 the impact velocity. Thus, the similarity of the crater shapes was completely confirmed.
258 Fig. 3c shows the crater profiles obtained at the impact velocity of $v_{\mathrm{i}} = 4.0$ km s^{-1}
259 for the projectiles with densities ranging from 14.9 to 1.2 g cm^{-3}. Both the diameter and
260 the depth of the craters became larger as the projectile density increased — except for the
261 PC projectile with its different diameter. Fig. 3c has been re-scaled by using the R_{rim}
262 values in order to show the normalized crater profiles in Fig. 3d. The normalized crater
263 profiles were very similar around only the crater rim, regardless of the projectile density,
264 but the normalized crater depth was deeper as the projectile density increased.
265 We analyzed the normalized crater profiles to determine the following parameters (Fig.
266 1c): the crater rim diameter (D_{rim}), the crater diameter measured on the pre-shot surface
267 (D_{c}), the crater depth from the rim peak to the crater bottom (d_{rim}), and the crater depth
268 from the pre-shot surface to the crater bottom (d_{c}). All of these parameters are explained
269 in Fig. 1c. The calculated ratio of the crater rim diameter to the crater diameter, $D_{\mathrm{rim}}/D_{\mathrm{c}}$,
270 was calculated to be 1.26 ± 0.04, regardless of the impact conditions. The ratio of the
271 crater depth to the crater diameter, $d_{\mathrm{c}}/D_{\mathrm{c}}$, is shown in Fig. 4. As mentioned above, the

Fig. 4

d_c/D_c increased with the increase of the projectile density, but it did not systematically depend on the impact velocity for each projectile. This d_c/D_c increase with the projectile density could have been caused by the penetration of the projectile into the target, because a high-density projectile penetrates deeper due to its greater momentum.

We were able to determine the precise crater diameter, D_c, by using the crater profiles obtained by the laser profiler, but the crater profile was not measured in all shots. The crater rim diameter, D_{rim}, was measured in all shots instead of the D_c. We thus used the following equation, $D_c = D_{rim}/1.26$, to construct the crater size scaling law. The experimental conditions and the crater size results are summarized in Table 2. Table 2

To study the relationship between π_4 and π_R in Eq. (4), we plotted the data for the same projectile diameter at a constant impact velocity (i.e., a constant π_2) in Fig. 5a. This Fig. 5 figure includes the data for seven projectiles (the exception is the PC projectile) with different densities at the impact velocity of 2 and 4 km s^{-1}. The π_R values increased slightly with the increase of π_4 at each impact velocity. This relationship can be described as follows:

$$\pi_R = 10^a \cdot {\pi_4}^b. \quad (5)$$

The coefficients of a and b were $a = 1.24 \pm 0.01$ and $b = 0.047 \pm 0.019$ for $v_i = 2$ km s^{-1}, and $a = 1.34 \pm 0.01$ and $b = 0.042 \pm 0.017$ for $v_i = 4$ km s^{-1}. The coefficient b was independent of the impact velocity, and its calculated average was 0.044. Therefore, the

291 power law index of π_2 in Eq. (4) can be determined from the relationship between $\pi_R \cdot$

292 $\pi_4{}^{-b}$ and π_2 in Fig. 5b as follows:

293 $$\pi_R \cdot \pi_4{}^{-b} = 10^{-0.265\pm0.014}\pi_2{}^{-0.176\pm0.002}. \quad (6)$$

294 The power law indices of the coupling parameters, μ and ν, in Eq. (4) were derived

295 from b and the power law index of π_2, and their values were μ =0.43 and ν =0.35.

296 The obtained μ was almost the same as that summarized by Housen and Holsapple

297 [2011] for sand targets based on the studies of Stöffler et al. [1975] and Cintala et al.

298 [1999]. Housen and Holsapple [2003] suggested that the typical value of ν could be

299 assumed to be 1/3. Our present finding is quite similar to this value.

300

301 *3.2. Impact-induced seismic waves*

302 We classified the impact-induced seismic waves observed in this study into two

303 categories depending on the distance from the impact point: (1) a single pulse-like wave

304 (Fig. 6a, b), and (2) a damped oscillation wave (Fig. 6c, d). The single pulse-like wave Fig. 6

305 usually appeared near the crater rim. Fig. 6a, b provides an example of a single pulse-like

306 wave obtained at the impact velocity of 5.2 km s^{-1} (run #140530-3). The acceleration

307 history in the range of time up to 100 ms is illustrated in Fig. 6a, and Fig. 6b shows the

308 history up to 15 ms. The time of '0 ms' corresponds to the time at which the projectile

309 impacted the target surface, which we determined from the high-speed digital camera

310 observation.

311 A complex wave with a small amplitude and a short wavelength was typically
312 observed after 50 ms from the impact (Fig. 6a). Our high-speed digital camera
313 observations revealed that many ejected grains from the crater dropped on the target
314 surface at ~ 50 ms after the impact. This complex wave could therefore also be generated
315 by the impact of grains dropped on the accelerometer. We then limited the seismic waves
316 to those that occurred during the first 30 ms for the analysis of these waveforms. The
317 single pulse-like wave was approximated by a damped oscillation wave with a large
318 damping rate, and the wave can thus be described as one cycle of a damped sinusoidal
319 curve with a frequency of several hundred Hz. The amplitude of the acceleration
320 attenuated with the propagation distance.

321 These features were very similar to those reported for an unconsolidated loose sand
322 target [McGarr et al., 1969] and those observed with a target of glass beads [Yasui et al.,
323 2015]. The damped oscillation wave usually appeared far from the crater rim. Fig. 6c, d
324 provide an example of the damped oscillation obtained at the impact velocity of 4.1 km
325 s^{-1} (run #150309–1); Fig. 6c shows the acceleration history in the range of time up to 200
326 ms, and Fig. 6d shows that up to 20 ms. A complex wave with a small amplitude and a
327 short wavelength was also observed after 100 ms of the impact (Fig. 6d). This complex
328 wave could also be generated by the impact of grains that fell on the accelerometer. The
329 distance between the accelerometer and the crater rim shown in Fig. 6c, d was greater

than the $x = 15$ cm of the accelerometer (Fig. 6a, b). It thus appears that the complex wave was generated by grains that fell at a later time. The seismic wave observed far from the crater rim is also approximated by a damped oscillation wave with a smaller damping rate as shown in Fig. 6c, d; the wave typically oscillated several times.

We analyzed these observed seismic waves to obtain three parameters characterizing them as expressed in Fig. 6e: the traveling time ($t_{\max}$), the maximum acceleration ($g_{\max}$), and the duration of the first upward acceleration (T_{half}). We used these parameters to determine the decay rate of the acceleration during the wave propagation. The experimental conditions and results including the data of three parameters are summarized in Tables 3–5. Table 3 concerns the PC projectile at the impact velocity of ~200 m s^{-1}, Table 4 is about the PC projectile at impact velocities >1 km s^{-1}, and Table 5 is the results for 2-mm projectiles with the projectile density ranging from 14.9 to 2.5 g cm^{-3} at impact velocities >1 km s^{-1}.

Table 3

Table 4

Table 5

3.3. Propagation velocity of impact-induced seismic waves

The traveling time of the impact-induced seismic wave ($t_{\max}$) is defined as the duration between the impact time and the time point at which the maximum acceleration of the first upward peak is observed. We used $t_{\max}$ to determine the propagation velocity of each impact-induced seismic wave on the target. Fig. 7a illustrates the relationship between the traveling time $t_{\max}$ and the propagation distance, x, for a PC projectile at

Fig. 7

350 the x from 5 cm to 30 cm at different impact velocities. The average crater rim radius at
351 each impact velocity is also shown on this figure as a horizontal line and in Table 6.

Table 6

352 The $t_{\max}$ value increases linearly with the increase of the x outside the crater rim
353 at each impact velocity, and thus the propagation velocity (V_{prop}) of the impact-induced
354 seismic waves could be constant outside the crater rim. We therefore calculated the V_{prop}
355 from the slope of this linear relationship, and each dataset corresponding to each impact
356 velocity was fitted by the linear equation. The V_{prop} obtained at each impact velocity is
357 shown in Table 6. Regardless of the impact velocity in the range from 7 to 0.2 km s^{-1}, the
358 V_{prop} values were almost constant within the error. The average V_{prop} was 51.1 ± 8.9 m
359 s^{-1}. The traveling time, $t_{\max}$, should be zero at the impact point of $x = 0$, but we
360 observed that all of the fitting lines had offsets at the intersection on the vertical axis at
361 $t = 0$ (Fig. 7a). The offset was larger as the impact velocity was higher. This offset was
362 also reported by Yasui et al. [2015], who suggested that the offset might be explained by
363 a high propagation velocity of an impact-induced seismic wave inside the crater rim.
364 At high-velocity impacts, the target around the impacted region was highly
365 compressed by a shock wave to achieve high pressure [Melosh, 1989], and the shock
366 wave propagated inside the crater. A shock wave velocity is experimentally known to
367 increase with the shock pressure, and therefore the traveling time inside the crater could
368 be dominated by the shock wave velocity, and then the large offset might be explained by
369 the short traveling time of the shock wave inside the crater. The $t_{\max}$ at the crater rim

370 for each impact velocity can be obtained by extrapolating each fitting line.

371 By using the $t_{\max}$ at the crater rim and the impact time ($t_{\max} = 0$ at $x = 0$), we
372 can speculate that the propagation velocity of an impact-induced seismic wave inside the
373 crater rim is about three times higher than that outside the crater rim, ~175 m s^{-1}. This
374 high velocity could be caused in part by the shock wave propagation inside the crater rim.
375 Fig. 7b delineates the relationship between the $t_{\max}$ and the x for 2-mm projectiles
376 with different densities at the impact velocity of 4 km s^{-1}. We suspected that this
377 relationship might move upward as the average crater rim radius becomes larger, and this
378 behavior was recognized at the other impact velocities. However, the slope of the linear
379 fitting line was almost the same, regardless of the projectile density. The V_{prop} obtained
380 for each projectile at each impact velocity is listed in Table 7. The average V_{prop} was Table 7
381 53.0 ± 6.4 m s^{-1}, which is almost the same as that for the PC projectile at different impact
382 velocities.

383 Yasui et al. [2015] measured the propagation velocity of impact-induced seismic
384 waves in glass beads with the mean diameter of 200 μm: 108.9 ± 16.2 m s^{-1}, which is
385 twice the velocity for the quartz sand obtained in the present experiments. They discussed
386 the effect of the frequency of the seismic wave on the propagation velocity, and they
387 concluded that the propagation velocity decreased with the decrease of the frequency. In
388 the present investigation, the measured frequency of the first peak was 700–100 Hz,
389 which is approximately one-half of the values reported by Yasui et al. [2015]. Thus, this

might be one of the reasons that the propagation velocity of quartz sand is smaller than that of glass beads. In addition, the grains of the quartz sand used herein have irregular shapes, differing sizes, and various angles of repose; these differences might also contribute to the low propagation velocity.

3.4. Maximum acceleration of impact-induced seismic waves

To examine the attenuation process of impact-induced seismic waves, we measured the maximum acceleration of the impact-induced seismic wave ($g_{\max}$) in our experiments. Fig. 8a clarifies the relationship between the $g_{\max}$ and the x for a PC projectile at the impact velocities from 7 to 0.2 km s^{-1}; the decay rate of the acceleration with the distance should be derived from this relationship. It is quite clear in the figure that the $g_{\max}$ attenuates with the x at each impact velocity, and the measured $g_{\max}$ was from 100 to 1 m s^{-2}. Thus, the $g_{\max}$ values can be fitted by the following power law equation:

Fig. 8

$$g_{\max} = 10^{a_r} \cdot x^{-b_r}, \qquad (7)$$

where a_r and b_r are constants, and b_r represents the attenuation rate of an impact-induced seismic wave. These values are provided in Table. 6. The slope b_r at the impact velocities from 7 to 4 km s^{-1} shows similar values from 3.1 to 2.5, whereas the b_r at the impact velocities from 3 to 0.2 km s^{-1} changed with the impact velocity and/or the distance from the impact point, from 3.8 to 1.1. In contrast, the a_r, which is related to the

409 magnitude of the absolute acceleration, depended to a slight extent on the impact velocity
410 as shown in Table. 6.

411 Fig. 8b shows the relationship between the $g_{\max}$ and the x obtained for different
412 projectiles at the constant impact velocity of 4 km s^{-1}. The measured $g_{\max}$ ranged from
413 40 to 1 m s^{-2}. Each data set for the different projectiles was fitted by Eq. (7). The obtained
414 a_r and b_r are shown in Table 7. The a_r value increased with the increase of the
415 projectile density, whereas the b_r value systematically changed with the projectile
416 density and was between 1.9 and 3.1. The obtained a_r and b_r values at different impact
417 velocities showed a similar relationship with the projectile density (Table 7). For each
418 projectile, the obtained a_r increased with the increase of the impact velocity, similar to
419 that observed for the PC projectile.

420 Yasui et al. [2015] clarified that the $g_{\max}$ was scaled well by using the distance from
421 the impact point normalized by the crater rim radius (x/R_{rim}) because the R_{rim} includes
422 all of the effects of the impact conditions according to the crater size scaling law described
423 in Eq. (6). This relationship between $g_{\max}$ and x/R_{rim} can be written as follows:

424 $$g_{\max} = 10^{a_n}(x/R_{\mathrm{rim}})^{-b_n}. \qquad (8)$$

425 Fig. 8c–e provides the $g_{\max}$ results expressed by the normalized distance, x/R_{rim}.
426 Panels (c) and (d) of Fig. 8 illustrate the data for a PC projectile and an Al projectile at
427 different impact velocities, respectively, and Fig. 8e is for all of the projectiles with

428 different projectile densities at different impact velocities. As seen in Fig. 8c, the data for
429 the 4.75-mm-dia. PC projectile are slightly scattered, and the data at 1 km s^{-1} are
430 somewhat smaller values than the others, but all of the $g_{\max}$ values obtained at different
431 impact velocities were well merged and could be scaled by the normalized distance.
432 Similarly, Fig. 8d (for a 2-mm-dia. Al projectile) demonstrates that all of the data were
433 merged well, and the relationship between $g_{\max}$ and the normalized distance was
434 independent of the impact velocity. The data for the other 2-mm-dia. projectiles showed
435 a similar tendency. Fig. 8e indicates that all of the data for the different projectiles merged
436 well, and this relationship was independent of both the impact velocity and the projectile
437 density. The data could be fitted by using Eq. (8), and the a_{n} and b_{n} were 2.21 ± 0.04
438 and 3.18 ± 0.10, respectively. From the empirical equation, the $g_{\max}$ at the crater rim
439 ($x/R_{\mathrm{rim}} = 1$) was estimated as 160 m s^{-2}; this value is approximately 16 times larger
440 than the Earth's gravity. At $g_{\max}$ =1 G, the normalized distance was estimated as 2.4.
441 The quartz sand in this region might have been fluidized by the impact-induced seismic
442 wave.
443 Yasui et al. [2015] measured the $g_{\max}$ of 200-μm glass beads for PC, alumina, and
444 SUS projectiles at impact velocities <150 m s^{-1}. The empirical equation fitted by Eq. (8)
445 is also shown in Fig. 8e. Comparing our results with those reported by Yasui et al., the
446 decay rate (b_{n}) of the quartz sand was approximately 1.5 times larger than that of the
447 glass beads. Surprisingly, the $g_{\max}$ of the quartz sand at the crater rim ($x/R_{\mathrm{rim}} = 1$)

448 was almost the same as that of the glass beads, i.e., ~150 m s^{-2}. We thus speculated that
449 the minimum acceleration necessary for crater excavation at the crater rim might be
450 approximately 15 G in the gravity regime for a crater formation process at the crater
451 diameters from 20 to 6 cm in this experiment. An excess acceleration beyond 1 G
452 corresponding to the fluidization of granular materials might be necessary to cause
453 excavation flow inside the crater rim.
454
455 *3.5. Duration of first upward acceleration*
456 The duration of the first upward acceleration could be explained by the generation
457 mechanism of impact-induced seismic waves. Yasui et al. [2015] defined the duration of
458 the first upward acceleration as a half-period of the first wave (T_{half}), which indicates the
459 length of time between the time point at which the acceleration rose from the background
460 level and the time point at which it fell back down to the background level.
461 Fig. 9a, b illustrates the relationship between the T_{half} and the distance from the Fig. 9
462 impact point: Fig. 9a is for a PC projectile at different impact velocities, and Fig. 9b is
463 for 2-mm-dia. projectiles with different densities at the impact velocity of 4 km s^{-1}. In
464 Fig. 9a, the data of the T_{half} are somewhat scattered but they are independent of the
465 distance from the impact point. The T_{half} results were somewhat dependent on the
466 impact velocity from 7 to 1 km s^{-1}, and the T_{half} at 200 m s^{-1} was clearly smaller than
467 the values at high impact velocities. Yasui et al. [2015] measured the T_{half} of 200-μm

468 glass beads at impact velocities <150 m s^{-1}. They reported a T_{half} of ~0.7 ms, which is
469 slightly smaller than that at 200 m s^{-1} and much smaller than the values obtained at high
470 impact velocities in our present experiments.

471 As shown in Fig. 9b, the T_{half} was independent of both the distance from the impact
472 point and the projectile density. The average T_{half} for the 2-mm-dia. projectiles at 4 km
473 s^{-1} was 2.01 ± 0.38 ms, which is approximately three times greater than that of glass beads.
474 In light of the data in these figures, we can say that the T_{half} increases with the increase
475 of the impact velocity, and it is independent of the projectile density. Our examination of
476 this tendency revealed the relationship between the T_{half} and the impact velocity for
477 each projectile (Fig. 9c). The data are slightly scattered and the error was not very small
478 for each result, but the T_{half} increased exponentially with the increase of the impact
479 velocity. Moreover, all of the data could be fitted by one empirical power law equation as
480 follows:

481 $$T_{\mathrm{half}}\,[\mathrm{ms}] = (1.65 \pm 0.11) \cdot (v_{\mathrm{i}}\,[\mathrm{km\ s^{-1}}])^{0.14\pm0.05}. \qquad (9)$$

482 Yasui et al. [2015] suggested that the T_{half} could be consistent with the duration of a
483 projectile penetration into the target. They calculated the penetration duration of the
484 projectile (t_{p}) by using the deceleration model proposed by Niimi et al. [2011]. They
485 chose the resistance law described by the dynamic pressure for a deceleration mechanism
486 in a hydrodynamic regime: $t_{\mathrm{p}} \propto {v_{\mathrm{i}}}^{-1}$. However, our experimental results cannot be

487 explained by this resistance law, because T_{half} is proportional to ${v_{\mathrm{i}}}^{0.14}$. We thus chose
488 another resistance law described by viscous drag force, as follows:

489 $$m_{\mathrm{p}}\frac{dv}{dt} = -A_0\eta r_{\mathrm{p}}v, \qquad (10)$$

490 where v is the projectile penetration velocity, t is the time, η is the viscosity of target
491 material, and A_0 is the constant related to the geometrical factor determined by an
492 experiment. The penetration duration of the projectile (t_{p}) could be obtained by the
493 following equations from the solution of Eq. (10) at $v = v_0$ (constant):

494 $$t_{\mathrm{p}} = -\tau \ln\left(\frac{v_0}{v_{\mathrm{i}}}\right) \qquad (11)$$

495 $$\tau = \frac{4\pi\rho_{\mathrm{p}}{r_{\mathrm{p}}}^2}{3A_0\eta}. \qquad (12)$$

496 The fitting line obtained by using Eq. (11) is also shown in Fig. 9c, and it can be seen that
497 Eq. (11) agrees with all of the data, as does Eq. (9). We can obtain the penetration velocity
498 just before the projectile stops (v_0) and the effective viscosity ($A_0\eta$) from Eqs. (11) and
499 (12): the v_0 was 1.8 m s^{-1}, regardless of the projectile properties, and the $A_0\eta$ increased
500 with the increase of the projectile density for the same projectile radius and the value was
501 40–240 Pas.

502

503 **4. Discussions**

504 *4.1. Impact-induced seismic energy propagating with distance*

505 The impact-induced seismic energy (E_{s}) is an important factor in evaluations of the

seismic shaking induced by the impact of small bodies on solid planets and asteroids. In this section, we estimate the E_s by using the empirical equations we obtained herein that describes the three parameters V_{prop}, g_{max}, and T_{half}. In the model proposed by Yasui et al. [2015], it is assumed that the E_s is the kinetic energy of the target material vibrating at the shell region, with a width corresponding to one cycle of the impact-induced seismic wave. The impact-induced seismic energy E_s is determined as follows:

$$E_s = \int_{x_1}^{x_2} \frac{1}{2} \cdot 2\pi x^2 \rho_t V(x,t)^2 dx, \qquad (13)$$

where ρ_t is the target density, x_1 and x_2 are the inside and outside distances of the shell region from the impact point, t is the time, and $V(x,t)$ is the vibration velocity of the target particle induced by the impact. For the estimation of E_s, it is difficult to use the original waveform of the acceleration obtained in the present study because the waveform had a complex shape, as shown in Fig. 6. Therefore, in order to calculate the $V(x,t)$, we simulated the impact-induced seismic wave (Fig. 10a). Fig. 10

The seismic wave has a positive phase and a negative phase (see Fig. 6), and a positive acceleration phase has a larger amplitude compared to a negative acceleration phase. We therefore divided the seismic wave into two regions: one region showing a half cycle of a sinusoidal wave with T_{half} and g_{max} in the positive amplitude region, and the other region with T_{2half} and g_{min} in the negative amplitude region. The acceleration in each region is expressed as follows:

$$a_{\mathrm{up}}(x,t) = g_{\max} \sin\left[\frac{\pi}{T_{\mathrm{half}}}\left(t - \frac{x}{V_{\mathrm{prop}}}\right)\right], \quad (14)$$

$$a_{\mathrm{down}}(x,t) = g_{\min} \sin\left[\frac{\pi}{T_{2\mathrm{half}}}\left\{t - \left(T_{\mathrm{half}} + \frac{x}{V_{\mathrm{prop}}}\right)\right\}\right], \quad (15)$$

where $a_{\mathrm{up}}(x,t)$ and $a_{\mathrm{down}}(x,t)$ are the acceleration in the positive and negative amplitude regions, respectively. The average V_{prop} obtained was 52.4 ± 7.2 m s^{-1}, regardless of the impact velocity and the projectile property. The $g_{\max}$ depended on the distance from the impact point normalized by the crater rim radius, x/R_{rim}, and it is expressed as Eq. (8). The $g_{\min}$ showing the maximum acceleration in the negative amplitude region could be obtained from our experimental results, and it is illustrated in Fig. 10b; the relationship between the absolute value of $g_{\max}/g_{\min}$ and the x/R_{rim} is shown. The $|g_{\max}/g_{\min}|$ had a good correlation with the x/R_{rim}, regardless of the projectile density and the impact velocity, and it can be expressed as the following power law equation:

$$|g_{\max}/g_{\min}| = 10^{1.09\pm0.03}(x/R_{\mathrm{rim}})^{-2.20\pm0.07}. \quad (16)$$

The T_{half} was slightly dependent on the impact velocity (v_{i}); it is expressed as Eq. (9). The vibration velocity of the target particle can be obtained by calculating the integral of Eqs. (14) and (15) for t, and it can be expressed as follows:

$$V_{\mathrm{up}}(x,t) = \frac{T_{\mathrm{half}}}{\pi} g_{\max}\left[1 - \cos\left\{\frac{\pi}{T_{\mathrm{half}}}\left(t - \frac{x}{V_{\mathrm{prop}}}\right)\right\}\right], \quad (17)$$

542 $$V_{\mathrm{down}}(x,t) = \frac{2T_{\mathrm{half}}}{\pi} g_{\max}$$

543 $$+ \frac{T_{2\mathrm{half}}}{\pi} g_{\min}\left[1 - \cos\left\{\frac{\pi}{T_{2\mathrm{half}}}\left(t - \left\{T_{\mathrm{half}} + \frac{x}{V_{\mathrm{prop}}}\right\}\right)\right\}\right]. \qquad (18)$$

544 Here, the $T_{2\mathrm{half}}$ was determined by the following boundary condition: $V_{\mathrm{down}}(x,$

545 $x/V_{\mathrm{prop}} + T_{\mathrm{half}} + T_{2\mathrm{half}}) = 0$. From this boundary condition, the $T_{2\mathrm{half}}$ can be

546 expressed as:

547 $$T_{2\mathrm{half}} = -T_{\mathrm{half}}\left(\frac{g_{\max}}{g_{\min}}\right), \qquad (19)$$

548 and Eq. (18) can be rewritten as follows:

549 $$V_{\mathrm{down}}(x,t) = \frac{T_{\mathrm{half}}}{\pi} g_{\max}\left[1 + \cos\left\{-\frac{\pi}{T_{\mathrm{half}}}\left(\frac{g_{\max}}{g_{\min}}\right)\left(t - \left\{T_{\mathrm{half}} + \frac{x}{V_{\mathrm{prop}}}\right\}\right)\right\}\right]. \qquad (20)$$

550 Fig. 11a–c presents an example of the original waveform obtained in this experiment Fig. 11

551 and the simulated waveforms calculated by using the Eqs. (14), (15), (17), and (20) for

552 the 2-mm-dia. Al projectile at the impact velocity of 4.14 km s^{-1} (run #151105–3). Fig.

553 11d clarifies the relationship between the vibration velocity, $V(x,t)$, and the distance

554 from the impact point normalized by the crater rim radius x/R_{rim} at different times from

555 18.0 to 7.5 ms. The maximum $V(x,t)$ decreased with the increase of the time. In

556 addition, the normalized distance at the maximum $V(x,t)$, i.e., $x_{\mathrm{peak}}/R_{\mathrm{rim}}$, increased

557 with the increase of the time.

558 The x_1 and x_2 values of Eq. (13) can be obtained from this relationship: they can

559 be calculated at the $V(x,t) = 0$ for each time. The impact-induced seismic energy (E_{s})

560 can be calculated by substituting Eqs. (17) and (20) into Eq. (13) with x_1 and x_2. Fig.

561 12a shows the relationship between the impact-induced seismic energy normalized by the
562 projectile kinetic energy, E_s/E_k, and the normalized distance at the maximum $V(x,t)$,
563 i.e., x_{peak}/R_{rim}, in the range of x_{peak}/R_{rim} from 1 to 10 at various impact conditions.
564 The E_s/E_k depends on the impact velocity and the projectile size and density. For
565 example, the E_s/E_k for a PC projectile at 200 m s^{-1} was more than 10 times larger than
566 that at 7 km s^{-1}, and the E_s/E_k for an Al projectile (2.7 g cm^{-3}) was twice as large as
567 that for a WC projectile (14.9 g cm^{-3}) at 4 km s^{-1}.

568 The E_s/E_k continued to decrease with the increase of the normalized distance
569 x_{peak}/R_{rim}, following the power law relationship of $E_s/E_k \propto (x_{peak}/R_{rim})^{-4.5}$. This
570 continuous decrease of the E_s/E_k could be caused by the energy dissipation in the plastic
571 wave. The impact generates a detached stress wave, initially as a strong shock wave, that
572 propagates away from the impact point, decays in magnitude, and eventually becomes an
573 elastic seismic wave. When the stress wave is in the shock and plastic regimes it loses the
574 energy rapidly with the normalized distance. On the other hand, once the stress wave
575 becomes an elastic wave, the energy losses should be small.

576 Thus, the elastic seismic wave did not appear in these experimental conditions, and
577 the impact-induced seismic efficiency factor could not be determined because the impact-
578 induced seismic efficiency factor is the E_s/E_k that ends up in the seismic/elastic wave
579 that can propagate large distances from the impact point. We expect that the E_s/E_k
580 continues to decrease until the plastic wave changes to the elastic wave, and then the

581 E_s/E_k becomes constant. Therefore, our obtained E_s/E_k could be the upper limit of the
582 impact-induced seismic efficiency factor.

583 We compared the E_s/E_k values obtained in this study with the reported impact-
584 induced seismic efficiency factor from previous experiments. For example, McGarr et al.
585 [1969] examined the seismic impulse normalized by the kinetic energy of a projectile,
586 I/E_k (which is similar to our E_s/E_k parameter) for a loose sand target at impact
587 velocities from 7 to 2 km s^{-1} in laboratory experiments. They obtained the average I/E_k
588 value of $(0.6 \pm 0.4) \times 10^{-5}$. We replotted their I/E_k values against the normalized
589 distance shown in Fig. 12a: we calculated the crater rim radius for each experiment in the
590 paper of McGarr et al. [1969] by using our crater size scaling law expressed by Eq. (6).
591 The McGarr et al. data then seemed to increase with the increase of the normalized
592 distance; this trend is the opposite of our results for each impact condition. As we
593 described above, the E_s/E_k depends on the impact velocity, and it could increase with
594 the decrease of the impact velocity.

Fig. 12

595 We thus presume that the increase of the I/E_k with the increase of the normalized
596 distance is not a true dependency on the distance; rather, it could be caused by the impact
597 velocity change from 7 to 2 km s^{-1}. If so, it might be possible that the I/E_k also decreases
598 with the increase of the normalized distance, because the maximum acceleration g_{max}
599 was observed to decrease with the normalized distance, x/R_{rim}, for the loose sand used
600 by McGarr et al. [1969] as shown in Fig. 12b. That is, their obtained seismic wave did

601 not also appear to be the elastic wave. Their obtained I/E_{k} might therefore correspond
602 to the upper limit of the impact-induced seismic efficiency factor, as is the case in our
603 present investigation. Their I/E_{k} value was larger than the values we obtained herein,
604 even though the impact velocity range was almost the same. The $g_{\max}$ for loose sand is
605 also greater than that for our quartz sand (Fig. 12b). This might be caused by differences
606 in mechanical properties of the target, such as the bulk sound velocity and the target
607 density.

608 Moore et al. [1970] carried out large-scale impact experiments using a missile at the
609 estimated impact velocity of 2.5 km s^{-1} at the White Sands Missile Range (New Mexico,
610 U.S.). The impact-induced seismic efficiency factor of 10^{-5} at the quite large kinetic
611 energy of the projectile, 4.5×10^{20} J, was obtained. In addition, Latham et al. [1970]
612 estimated the impact-induced seismic efficiency factor as 10^{-5} to 10^{-6} by using the lunar
613 module impact provided by the Apollo; the impact velocity of the lunar module was
614 estimated to be 1.7 km s^{-1} and the kinetic energy was 3.6×10^{11} J [Toksöz et al., 1974].
615 Their values are larger than our calculated $E_{\mathrm{s}}/E_{\mathrm{k}}$ at the normalized distances far from 6;
616 however, our values could be the upper limit of the impact-induced seismic efficiency
617 factor.

618 Herein, we measured the acceleration along the direction perpendicular to the target
619 surface. However, the particle motion induced by the seismic wave has not only a vertical
620 component (Z); the motion also has horizontal (X) and radial (Y) components in the target

621 (Fig. 13a). We thus measured the acceleration excited along these three axes by using a
622 triaxial accelerometer to confirm the amplitude of the acceleration along the X- and Y-
623 axes. Fig. 13b shows the acceleration measured at the X-, Y-, and Z-axes for a PC
624 projectile at 2.4 km s^{-1}. The triaxial accelerometer was set at 11 cm from the impact point
625 (x/R_{rim} =1.5). We observed that acceleration at the Y-axis was not detected.

Fig. 13

626 Based on the crater formation model proposed by Maxwell [1977], each flow line
627 drawn from an impact point never crosses another flow line, which means that the particle
628 motion does not have a radial component. This is the reason why the acceleration at the
629 Y-axis was not detected. In addition, we firstly observed that the maximum acceleration
630 at the X-axis was about five times larger than that at the Z-axis, and thus it is clear that
631 the kinetic energy of the particle is dominated by the horizontal motion. When we
632 calculate the particle velocity considering the acceleration along the X-axis, the
633 $E_{\mathrm{s}}/E_{\mathrm{k}}$ could be more than one order of magnitude larger than that calculated in Fig. 12a.
634 This is why our calculated $E_{\mathrm{s}}/E_{\mathrm{k}}$ was smaller than the impact-induced seismic
635 efficiency factor estimated from the missile experiments and the lunar module impact
636 [Moore et al., 1970; Latham et al., 1970]. In the future, in order to determine the impact-
637 induced seismic efficiency factor, it is necessary to measure the acceleration by using a
638 triaxial accelerometer at a distant region where the seismic wave changes to the elastic
639 wave.
640

4.2. Possibility of detecting an impact-induced seismic shaking on asteroids

To estimate the effects of impact-induced seismic shaking on asteroids, we used the empirical equations that we obtained in this study. These equations were obtained under Earth's gravity, 1 G, so we should consider the effect of microgravity when applying our established model to the resurfacing processes that are due to impact-induced seismic shaking on asteroid surfaces. As described next, we constructed an impact-induced seismic shaking model including the effect of gravity on asteroids by comparing our experimental results with the scaling law for ejecta velocity distribution, and we discuss the possibility of the impact-induced seismic shaking on asteroids.

We first consider the particle velocity ejected at the position of the crater radius in accord with the scaling law for ejecta velocity distribution that was proposed by Housen and Holsapple [2011]. The ejection velocity at the position of the crater radius, v_{e}, is written as follows:

$$v_{\mathrm{e}} = c_0\sqrt{gR_{\mathrm{c}}}, \qquad (21)$$

where g is the gravitational acceleration in m s^{-2} and c_0 is the constant determined by experiments for each target material. Next, we assume that the ejection velocity of a particle at the position of the crater radius ($x/R_{\mathrm{c}} = 1$) can be simply estimated by using the product of the maximum acceleration, $g_{\max}$, in Eq. (8), and the duration of the first upward acceleration, T_{half}. The maximum acceleration at $x/R_{\mathrm{c}} = 1$ is rewritten as

660 $g_{\max} = (1.26)^{b_n} g_0$ under a certain gravity, where $R_c = R_{rim}/1.26$ and g_0 is the
661 maximum acceleration at the crater rim. Thus, the ejection velocity can be written as
662 follows:

663 $$v_{e\perp}[\mathrm{m\ s^{-1}}] = g_{\max} \cdot T_{half} = (1.26)^{b_n} g_0 T_{half}, \qquad (22)$$

664 where $v_{e\perp}$ is the ejection velocity of the particles in the normal direction. It is assumed
665 that the target particles are ejected from the target surface with the ejection angle of 45°,
666 a typical ejection angle of granular materials [e.g., Tsujido et al., 2015], and it is assumed
667 that the ejection velocity estimated from the scaling law of Eq. (21) is equal to be that
668 obtained in this experiment as Eq. (22). Thus, the ejection velocity of the particles at
669 $x/R_c = 1$ can be rewritten as $v_e = \sqrt{2} v_{e\perp}$, and the following equation is constructed by
670 using Eqs. (21) and (22):

671 $$c_0 \sqrt{g R_c} = \sqrt{2} \times (1.26)^{b_n} g_0 T_{half}, \qquad (23)$$

672 that is,

673 $$g_0 = \frac{c_0 (1.26)^{-b_n}}{\sqrt{2}} \times \frac{\sqrt{g R_c}}{T_{half}}. \qquad (24)$$

674 The R_c is calculated from the crater size scaling law of Eq. (6) and is shown as follows:

675 $$R_c = (8.75 \times 10^{-1}) g^{-0.176} {v_i}^{0.352} {r_p}^{0.824} \left(\frac{\rho_t}{\rho_p}\right)^{-0.289}, \quad (25)$$

676 where the projectile mass, m_p, can be written as $4\pi\rho_p {r_p}^3/3$ by assuming a spherical

677 shape. Therefore, the g_0 can be rewritten as follows:

678 $$g_0 = \frac{(3.17 \times 10^{-1}) c_0 (g r_\mathrm{p})^{0.412} v_\mathrm{i}^{0.176} (\rho_\mathrm{t}/\rho_\mathrm{p})^{-0.145}}{T_\mathrm{half}}, \quad (26)$$

679 where b_n =3.18 in Eq. (8). To compare our semi-theoretical equation for g_0 with the
680 obtained g_0, which is 10^{a_n} (a_n =2.21 ± 0.04) in Eq. (8), in our experiments, we used
681 the T_half of the empirical equation, Eq. (9). Substituting Eq. (9) into Eq. (26), the g_0
682 can be rewritten as follows:

683 $$g_0 = (3.97 \times 10^{2}) (g r_\mathrm{p})^{0.412} v_\mathrm{i}^{0.036} \left(\frac{\rho_\mathrm{t}}{\rho_\mathrm{p}}\right)^{-0.145}, \quad (27)$$

684 where c_0 =0.76 m s^{-1} as obtained by Tsujido et al. [2015]. Fig. 14 shows the Fig. 14
685 calculated results of Eq. (27) at the impact velocity (v_i) of 0.2–7 km s^{-1} for various
686 projectiles. The gray zone shown in Fig. 14 represents the 10^{a_n} in Eq. (8), and all of the
687 calculated g_0 values were a little smaller than the observed g_0 (10^{a_n} in Eq. (8)). The
688 difference between the calculated g_0 values and the observed g_0 might be caused by
689 the ejection angle and/or the duration, T_half. The g_0 was measured below the target
690 surface (2.5 cm from the target surface) in our experiments while the calculated g_0 was
691 estimated on the target surface. Therefore, the g_0 might depend on the depth from the
692 target surface. However, their differences were within a factor of 2 and they were
693 consistent within error bars. Our semi-theoretical equation of Eq. (26) could be suitable
694 for the estimation of g_0 at various impact conditions.

695 Although the $g_{\max}$ at the crater rim, that is, the g_0 was very similar in all of our
696 experiments, the semi-theoretical equation of Eq. (26) suggests that the g_0 is sensitive
697 to the product of surface gravity and the projectile radius. In our experiments, the
698 projectile radius was changed by a factor of 2, and thus an effect of the projectile radius
699 on the g_0 was not recognized. This result should be verified by future experiments
700 and/or numerical simulations.

701 Lastly, we considered the impact-induced seismic shaking on an idealized small (500
702 m in diameter) body with a bulk density of 1.46 g cm^{-3}, which is the same as our target.
703 In this calculation, we should include the effect of the impactor size on the T_{half} of Eq.
704 (26), and we therefore used the theoretical equations of Eqs. (11) and (12). Substituting
705 Eqs. (11) and (12) into Eq. (26), the g_0 can be rewritten as follows:

706 $$g_0 = -(5.79 \times 10^{-2})(A_0\eta)\left(gr_{\mathrm{p}}\right)^{0.412} {v_{\mathrm{i}}}^{0.176} {r_{\mathrm{p}}}^{-2} {\rho_{\mathrm{t}}}^{-0.145} {\rho_{\mathrm{p}}}^{-0.856} \left[\ln\left(\frac{v_0}{v_{\mathrm{i}}}\right)\right]^{-1}, \quad (28)$$

707 where $c_0 = 0.76$ m s^{-1} obtained by Tsujido et al. [2015], and $A_0\eta$ and v_0 were
708 determined by our experiments using PC projectiles. The $A_0\eta$ and v_0 values were 114
709 Pas and 1.3 m s^{-1}, respectively. In this calculation, the impactors with the diameter of
710 0.01, 0.1, 0.5, and 1 m and the density of 1.4 g cm^{-3} (which is the average density of C-
711 type asteroids as shown by Britt et al. [2002]) were assumed to collide at the impact
712 velocity of 5 km s^{-1}, a typical collisional velocity in the region of main belt. We then
713 calculated the maximum acceleration attenuated with the distance calculated for the

different sizes of the impactor by using Eq. (8), i.e., $g_{\max} = g_0(x/R_{\mathrm{rim}})^{-3.18}$.

Fig. 15 illustrates the relationship between the distance from the impact point normalized by the crater rim radius, x/R_{rim}, and the maximum acceleration, $g_{\max}$. The region at which the impact-induced seismic shaking occurred was assumed to be within the distance from the impact point corresponding to the $g_{\max}$ beyond the surface gravity of the idealized small body. The $g_{\max}$ was observed to increase with the decrease of the impactor size at the same normalized distance. The $g_{\max}$ with the impactor size of 0.01 m at $x/R_{\mathrm{rim}} = 1$ was more than three orders of magnitude larger than that obtained with a 1-m impactor.

Fig. 15

The area at which the impact-induced seismic shaking occurred changed with the impactor size. The normalized distance at which the impact-induced seismic shaking occurred changed from 9 to 0.9 when the impactor size increased from 0.01 m to 1 m. When an impact crater with a rim diameter of 2.8 m is formed by a 0.01-m impactor on this idealized small body, impact-induced seismic shaking could be induced within the distance of 12 m from the impact point. However, when a crater with a diameter of 123 m is formed by a 1-m impactor, the region at which the impact-induced seismic shaking occurs could be limited to within the crater rim, and thus the seismic shaking will not occur far from the crater.

5. Summary

734 We carried out impact cratering experiments using eight types of spherical projectiles
735 with density ranging from 14.9 to 1.2 g cm^{-3} on 500-μm quartz sand at the impact velocity
736 from 7 to 0.2 km s^{-1}. We examined the waveform of the acceleration generated just after
737 the impact, and we assessed the characteristics of the impact-induced seismic wave by
738 using three to five accelerometers set at 5.1 to 30.1 cm from the impact point in order to
739 consider the possibility of impact-induced seismic shaking on asteroids. Our results are
740 summarized as follows:

741 1. We applied our results obtained under various impact conditions (e.g., the projectile
742 size, projectile density, and impact velocity) to the crater size scaling law proposed
743 by Housen and Holsapple [2011], and we determined the following empirical
744 equation, $\pi_{\mathrm{R}} \cdot {\pi_4}^{-0.044} = 10^{-0.265} {\pi_2}^{-0.176}$, where π_{R}, π_2, and π_4 are the non-
745 dimensional scaling parameters related to the crater rim radius, gravity, impact
746 velocity, projectile density, and target density. We obtained the power law indices of
747 the coupling parameters, μ and ν, as 0.43 and 0.35, respectively.

748 2. The propagation velocity of an impact-induced seismic wave, V_{prop}, was determined
749 by using the duration between the impact time and the time showing the maximum
750 acceleration of the first upward peak. The obtained V_{prop} was 52.4 ± 7.2 m s^{-1}
751 outside the crater, regardless of the impact velocity and the projectile properties. The
752 V_{prop} inside the crater rim was speculated to be ~175 m s^{-1}, which is approximately
753 three times larger than that outside the crater rim.

3. The maximum acceleration of the impact-induced seismic wave, $g_{\max}$, could be scaled as the distance from the impact point normalized by the crater rim radius, x/R_{rim}, regardless of the impact velocity and the projectile properties, and the obtained empirical equation was shown as $g_{\max} = 10^{2.21} \cdot (x/R_{\mathrm{rim}})^{-3.18}$. The $g_{\max}$ of quartz sand at the $x/R_{\mathrm{rim}} = 1$ obtained in this study matched well with that of the 200-μm glass beads reported by Yasui et al. [2015].

4. The duration of the first upward acceleration was defined as a half period of the first upward wave, T_{half}, and we observed that T_{half} was slightly dependent on the impact velocity but independent of the projectile properties. The obtained empirical equation was $T_{\mathrm{half}}\,[\mathrm{ms}] = 1.65(v_{\mathrm{i}}\,[\mathrm{km\ s^{-1}}])^{0.14}$. Our obtained T_{half} could be explained by the resistance law described by viscous drag force.

5. We calculated the seismic energy normalized by the kinetic energy of the projectile, $E_{\mathrm{s}}/E_{\mathrm{k}}$, by using our obtained empirical equations at the normalized distance from $x/R_{\mathrm{rim}} = 1$ to 10 under various impact conditions. The $E_{\mathrm{s}}/E_{\mathrm{k}}$ depended on the impact velocity and projectile properties, but the decay constant was approximately 4.5, regardless of the impact condition.

6. We estimated the distance from the crater rim at which the impact-induced seismic shaking occurred on an idealized small (500 m in diameter) body by using our semi-theoretical equation. When we assumed the impact velocity of the impactor to be 5 km $\mathrm{s^{-1}}$, the impact-induced seismic shaking area could be calculated for various

774 impactor sizes.

Acknowledgments

We appreciate the great help with our experiments provided by Ms. S. Tsujido and Mr. S. Takano of Kobe University. We are grateful to Prof. G. Collins, Imperial College London, and the anonymous reviewer for many useful suggestions and corrections that helped us to improve this paper. Our series of experiments were supported in part by the Hypervelocity Impact Facility at ISAS/JAXA. This work was supported in part by Grants-in-Aid for Scientific Research (no. 16H04041, no. 16K17794, and no. 19H00719) from the Japan Ministry of Education, Culture, Sports, Science and Technology.

Reference

Asphaug, E., Melosh, H. J., 1993. The Stickney impact of Phobos: A dynamical model. Icarus 101, 144–164.

Britt, D. T., Yeoman, D., Housen, K., Consolmagno, G., 2002. Asteroid density, porosity, and structure. In: Bottke, W.F., Cellino, A., Paolicchi, P., Binzel, R. (Eds.), Asteroids III. Univ. Arizona Press, Tucson, AZ, pp. 485−500.

Cheng, A. F., Izenberg, N., Chapman, C. R., Zuber, M. T., 2002. Ponded deposits on asteroid 433 Eros. Meteorit. Planet. Sci. 37, 1095–1105.

Cintala, M. J., Berthoud, L., Hörz, F., 1999. Ejection-velocity distributions from impacts into coarse-grained sand. Meteorit. Planet. Sci. 34, 605–623.

Collins, G. S., Melosh, H. J., Marcus, R. A., 2005. Earth impact effects program: A web-

795 based computer program for calculating the regional environmental consequences of
796 a meteoroid impact on Earth. Meteorit. Planet. Sci. 40, 817–840.
797 Gault, D. E., Heitowit, E. F., 1963. The partition of energy for hypervelocity impact
798 craters formed in rock. In: Proc. Sixth Hypervelocity Impact Symp. 2, pp. 419-456.
799 Greenberg, R., Nolan, M. C., Bottke Jr., W. F., Kolvoord, R. A., Veverka, J., 1994.
800 Collisional history of Gaspra. Icarus 107, 84–97.
801 Greenberg, R., Bottke, W. F., Nolan, M., Geissler, P., Petit, J. -M., Durda, D. D., Asphaug,
802 E., Head, J., 1996. Collisional and dynamical history of Ida. Icarus 120, 106–118.
803 Güldemeister, N., Wünnemann, K., 2017. Quantitative analysis of impact-induced
804 seismic signals by numerical modeling. Icarus 296, 15–27.
805 Holsapple, K. A., 1993. The scaling of impact processes in planetary sciences. Annu. Rev.
806 Earth Planet. Sci. 21, 333–373.
807 Housen, K. R., Holsapple, K. A., 2003. Impact cratering on porous asteroids. Icarus 163,
808 102–119.
809 Housen, K. R., Holsapple, K. A., 2011. Ejecta from impact craters. Icarus 211, 856–875.
810 Latham, G., Ewing, M., Dorman, J., Press, F., Toksoz, N., Sutton, G., Meissner, R.,
811 Duennebier, F., Nakamura, Y., Kovach, R., Yates, M., 1970. Seismic data from man-
812 made impacts on the Moon. Science 170, 620–626.
813 Maxwell, D. E., 1977. Simple Z model of cratering, ejection, and the overturned flap. In:
814 Roddy, D.J., Pepin, R.O., Merrill, R.B. (Eds.), Impact and Explosion Cratering.

815 Pergamon, NY, pp. 1003–1008.
816 Melosh, H. J., 1989. Impact Cratering: A Geologic Process. Oxford Univ. Press, New
817 York, pp. 253.
818 McGarr, A., Latham, G. V., Gault, D. E., 1969. Meteoroid impacts as sources of seismicity
819 on the Moon. J. Geophys. Res. 74, 5981–5994.
820 Miyamoto, H., Yano, H., Scheeres, D. J., Abe, S. et al., 2007. Regolith migration and
821 sorting on asteroid Itokawa. Science 316, 1011–1014.
822 Moore, H. J., Latham, G. V., McDonald, W. G., 1970. Missile impacts as sources of
823 seismic energy on the moon. Science 168, 242–244.
824 Niimi, R., Kadono, T., Arakawa, M., Yasui, M., Dohi, K., Nakamura, A. M., Iida, Y.,
825 Tsuchiyama, A., 2011. In situ observation of penetration process in silica aerogel:
826 Deceleration mechanism of hard spherical projectiles. Icarus 211, 986–992.
827 Richardson Jr., J. E., Melosh, H. J., Greenberg, R. J., O'Brien, D. P., 2005. The global
828 effects of impact-induced seismic activity on fractured asteroid surface morphology.
829 Icarus 179, 325–349.
830 Robinson, M. S., Thomas, P. C., Veverka, J., Murchie, S. L., Wilcox, B. B., 2002. The
831 geology of 433 Eros. Meteor. Planet. Sci. 37, 1651–1684.
832 Shishkin, N. I., 2007. Seismic efficiency of a contact explosion and a high-velocity impact.
833 J. App. Mech. Tech, Phys. 48, 145–152.
834 Stöffler, D., Gault, D. E., Wedekind, J., Polkowski, G., 1975. Experimental hypervelocity

impact into quartz sand: Distribution and shock metamorphism of ejecta. J. Geophys. Res. 80, 4062–4077.

Thomas, P. C., Joseph, J., Carcich, B., Veverka, J. et al., 2002. Eros: Shape, topography, and slope processes. Icarus 155, 18–37.

Toksöz, M. N., Dainty, A. M., Solomon, S. C., Anderson, K. R., 1974. Structure of the Moon. Rev. Geophys. Space Phys. 12, 539–567.

Tsujido, S., Arakawa, M., Suzuki, A. I., Yasui, M., 2015. Ejecta velocity distribution of impact craters formed on quartz sand: Effect of projectile density on crater scaling law. Icarus 262, 79–92.

Veverka, J., Thomas, P. C., Robinson, M., Murchie, S. et al., 2001. Imaging of small-scale features on 433 Eros from NEAR: Evidence for a complex regolith. Science 292, 484–488.

Wójcicka, N., Collins, G. S., Bastow, I., Miljković, K., Teanby, N. A., Karakostas, F., Lognonné, P., the InSight Team., 2019. Investigating the relationship between the seismic efficiency and seismic moment and impactor properties on Mars. In: Proceedings of the 50th Lunar and Planetary Science Conference, #2633.

Yasui, M., Matsumoto, E., Arakawa, M., 2015. Experimental study on impact-induced seismic wave propagation through granular materials. Icarus 260, 320–331.

853 **Figure Captions:**

854

855 **Figure 1**

856 Schematic illustration of the experimental setup. (a) Two-stage vertical gas gun. (b) Five
857 accelerometers set on the target surface. (c) Cross-section of the accelerometers set on the
858 target surface, and an illustration of the crater dimensions.

859

860 **Figure 2**

861 Impact craters on the quartz sand target. (a) The PC projectile at 1.13 km s^{-1}, run
862 #151104–3. (b) The PC projectile at 6.89 km s^{-1}, run #141003–2, which was the largest
863 impact crater in this study. (c) The Al projectile at 4.12 km s^{-1}, run #150309–1. (d) The
864 Cu projectile at 3.63 km s^{-1}, run #150820–5. Each scale bar indicates 5.0 cm. The thick
865 black lines around the crater rim are the accelerometers' cords.

866

867 **Figure 3**

868 Crater profiles obtained at different impact conditions. (a) The results obtained with the
869 PC projectile at the impact velocities of 1.1, 2.2, 4.2, and 6.2 km s^{-1}. (b) The crater
870 profiles expressed by the relationship between the values of x/R_{rim} and the y/R_{rim} for
871 panel (a). (c) The results of the projectiles with different densities at the impact velocity
872 of ~ 4.0 km s^{-1}. (d) The crater profile expressed by the relationship between the x/R_{rim}

873 and the y/R_{rim} for panel (c).

874

875 **Figure 4**

876 The relationship between the ratio of the crater depth to the crater diameter, $d_{\mathrm{c}}/D_{\mathrm{c}}$, and
877 the projectile density. Each symbol indicates an impact velocity range.

878

879 **Figure 5**

880 (a) The relationship between the non-dimensional scaling parameter π_4 and the π_{R}
881 defined in Eqs. (1) and (2). The results were obtained by the experiments using seven
882 projectiles with different densities at a constant impact velocity of 2.0 km s^{-1}
883 (circles) and 4.0 km s^{-1} (squares). The solid and dashed lines represent the fitting
884 lines determined by using the power law equation of Eq. (5).
885 (b) The relationship between the non-dimensional scaling parameter π_2 and the $\pi_{\mathrm{R}} \cdot$
886 ${\pi_4}^{-b}$ (in this study, we obtained b =0.044). The solid line represents the fitting line
887 determined by using the power law equation of Eq. (6).

888

889 **Figure 6**

890 (a) A typical sample of the impact-induced seismic wave showing a single pulse-like
891 wave observed in this study. A PC projectile was impacted at the velocity of 5.16 km
892 s^{-1} (run #140530–3). The three different curves represent the data recorded by three

accelerometers set at different distances from the impact point, x. Time 0 is the impact time of the projectile.

(b) Enlargement of the horizontal axis of panel (a) ranging from -2 to 15 ms.

(c) An example of the impact-induced seismic wave showing a damped vibration wave observed far from the crater rim. An Al projectile was impacted at the velocity of 4.12 km s^{-1} (run #150309–1).

(d) Enlargement of the horizontal axis of panel (c) ranging from -2 to 20 ms.

(e) The physical properties of an impact-induced seismic wave: the traveling time ($t_{\max}$), the maximum acceleration ($g_{\max}$), and the duration of the first upward wave of the acceleration (T_{half}).

Figure 7

The relationship between the traveling time ($t_{\max}$) and the distance from the impact point, x (a) for PC projectile at different impact velocities, and (b) for 2-mm projectiles with different densities at the impact velocity of 4 km s^{-1}. Horizontal lines represent the average crater rim radius at each impact velocity. The fitting lines were obtained by using a linear function.

Figure 8

(a, b) The relationship between the maximum acceleration ($g_{\max}$) and the distance from

913 the impact point, x (a) for PC projectile at impact velocities ranging from 7 to 0.2
914 km s^{-1} and (b) for 2-mm projectiles with the projectile density ranging from 14.9 to
915 2.5 g cm^{-3} at the impact velocity of 4 km s^{-1}. Each line represents the fitting line
916 obtained by using Eq. (7).
917 (c–e) The relationship between the maximum acceleration ($g_{\max}$) and the distance from
918 the impact point normalized by the crater rim radius, x/R_{rim} (c) for PC projectile
919 at impact velocities from 7 to 0.2 km s^{-1}, (d) for Al projectile at impact velocities
920 from 5 to 2 km s^{-1}, and (e) for all data. The solid and dashed lines in panel (e)
921 represent the fitting lines obtained by using Eq. (8) and the empirical equation used
922 for 200-μm glass beads obtained by Yasui et al. [2015], respectively.
923
924 **Figure 9**
925 (a, b) The relationship between the duration of the first upward acceleration (T_{half}) and
926 the distance from the impact point, x (a) for PC projectile at impact velocities from
927 7 to 0.2 km s^{-1} and (b) for 2-mm projectiles with the projectile density from 14.9 to
928 2.5 g cm^{-3} at the impact velocity of 4.0 km s^{-1}. The solid line in panel (b), and the
929 dotted line and gray area in panels (a) and (b) represent the average values for all of
930 the data obtained in this study, that for the 200-μm glass beads used by Yasui et al.
931 [2015], and the standard deviation for each data set, respectively.
932 (c) The average T_{half} at each impact velocity for all projectiles. The solid and dashed

933 lines represent the fitting lines obtained by using Eqs. (9) and (11), respectively.

934

935 **Figure 10**

936 (a) Schematic of a simulated impact-induced seismic wave for Eqs. (14) and (15).

937 (b) The relationship between the absolute ratio of the maximum acceleration in the
938 positive amplitude region to that in the negative amplitude region, i.e., $|g_{\max}/g_{\min}|$,
939 and the normalized distance, x/R_{rim} for various projectiles. The solid line represents
940 the fitting line obtained with Eq. (16).

941

942 **Figure 11**

943 (a) Waveforms of acceleration measured at $x =$ 10.7, 13.0, 15.4, 18.1, and 22.4 cm from
944 the impact point, (run #151105–3).

945 (b) The relationship between the acceleration, a, and the time in ms, calculated by using
946 Eqs. (14) and (15) under the same impact conditions as those in panel (a). The
947 numbers in the legend represent the x/R_{rim}.

948 (c) The relationship between the vibration velocity, V, and the time in ms, calculated
949 with Eqs. (17) and (20) under the same impact conditions as those in panel (a). The
950 numbers in the legend represent the x/R_{rim}.

951 (d) The relationship between the vibration velocity, V, and the distance from the impact
952 point normalized by the crater rim radius, x/R_{rim}, calculated with Eqs. (17) and (20)

under the same impact conditions as those in panel (a). The numbers in the legend represent the elapsed times.

Figure 12

(a) The relationship between the seismic energy normalized by the kinetic energy of the projectile, E_s/E_k, and the distance from the impact point normalized by the crater rim radius at the maximum vibration velocity, x_{peak}/R_{rim}, on Fig. 11d under various impact conditions. The open symbols represent the data of loose sand obtained by McGarr et al. [1969].

(b) The relationship between the maximum acceleration, g_{max}, and the distance from the impact point normalized by the crater rim radius, x/R_{rim}. This figure is same as Fig. 8e. The solid circles represent the data of loose sand from McGarr et al. [1969].

Figure 13

(a) Cross-section of the triaxial accelerometer setting on the target surface. The X-, Y-, and Z-vectors indicate the directions of the measured acceleration.

(b) Impact-induced seismic waves at the three orthogonal directions measured by the triaxial accelerometer set at 11 cm from the impact point for a PC projectile at the impact velocity of 2.4 km s^{-1}: the crater rim radius is 7.5 cm.

973 **Figure 14**

974 Comparison of the g_0 values calculated using the semi-theoretical equation of Eq. (27)
975 for various impact conditions (symbols) with those obtained in our experiments (gray
976 zone).

977

978 **Figure 15**

979 The relationship between the maximum acceleration, $g_{\max}$, and the distance from the
980 impact point normalized by the crater rim radius, x/R_{rim}, for an impactor with a density
981 of 1.4 g cm^{-3} at the impact velocity of 5 km s^{-1} on an idealized small (500 m in diameter)
982 body and a 1.46 g cm^{-3} density. The thick lines represent the results calculated with Eqs.
983 (8) and (28) with impactor diameters from 0.01 to 1 m. The horizontal dotted line shows
984 the surface gravity of the idealized small body. The number in each parenthesis represents
985 the crater rim radius.

986 Table 1. Experimental conditions and results on the morphology of impact crater

Run number	Projectile	v_i, m s^{-1}	D_{rim}, cm	D_c, cm	d_{rim}, cm	d_c, cm	D_{rim}/D_c	d_c/D_c
150819-3	PC	4230	17.7	13.1	3.8	3.0	1.36	0.23
151104-1	PC	2208	13.7	10.7	2.6	2.1	1.29	0.20
151104-2	PC	6150	20.2	16.0	4.1	3.5	1.26	0.22
151104-3	PC	1125	11.2	8.6	2.3	2.0	1.30	0.23
151105-2	PC	1206	11.7	9.2	2.0	1.6	1.27	0.17
150610-1	Al	1994	8.2	6.3	1.4	1.1	1.30	0.17
150611-3	Al	5015	12.1	9.5	2.8	2.4	1.28	0.26
150612-1	Al	1815	8.2	6.3	1.3	0.9	1.31	0.15
150612-2	Al	2062	8.6	7.0	1.2	0.9	1.24	0.13
150820-1	Al	2920	9.5	7.2	1.5	1.2	1.32	0.16
150820-7	Al	3953	10.8	8.4	1.5	1.2	1.29	0.14
151105-3	Al	4143	10.6	8.2	1.8	1.3	1.29	0.16
150611-5	Gl	5318	11.5	9.3	1.8	1.4	1.24	0.15
150611-6	Gl	2281	8.6	6.9	1.4	1.1	1.25	0.16
150612-5	Gl	2023	8.4	7.0	1.3	1.1	1.19	0.16
150820-2	Gl	4023	10.5	8.4	1.9	1.6	1.24	0.19
150821-1	Gl	3427	10.2	7.9	1.7	1.3	1.28	0.16
150821-2	Gl	4013	10.5	8.6	1.5	1.2	1.23	0.14
150820-3	Ti	3834	11.9	9.8	2.1	1.7	1.21	0.17
150821-3	Ti	2044	10.3	8.2	1.9	1.6	1.25	0.20

150821-5	Ti	1972	10.0	7.7	1.9	1.6	1.29	0.20
160720-1	Ti	5181	13.4	11.0	2.1	1.8	1.22	0.16
150820-4	ZrO_2	3934	13.3	11.4	2.8	2.5	1.17	0.22
160719-3	ZrO_2	2153	10.8	8.5	2.0	1.6	1.27	0.19
160720-2	ZrO_2	5727	14.7	11.3	2.9	2.4	1.28	0.21
150610-2	SUS	1841	11.3	8.9	2.6	2.2	1.26	0.25
150611-4	SUS	4936	15.8	12.7	4.1	3.7	1.24	0.29
150612-3	SUS	1848	11.0	8.7	2.7	2.3	1.27	0.27
150612-4	SUS	1824	10.9	8.6	2.7	2.3	1.26	0.27
150820-6	SUS	3805	14.2	11.9	3.1	2.7	1.20	0.23
150820-5	Cu	3626	14.4	11.7	3.7	3.2	1.23	0.27
151105-1	Cu	2114	11.9	9.8	3.1	2.8	1.22	0.29
160719-1	Cu	2238	12.4	9.8	2.9	2.4	1.27	0.25
160720-4	Cu	5348	15.8	12.3	2.7	2.2	1.29	0.18
160721-3	Cu	2306	12.5	10.3	2.6	2.2	1.22	0.22
150819-4	WC	3422	16.6	13.6	4.1	3.6	1.22	0.26

987 D_{rim}: Crater rim diameter

988 D_{c}: Crater diameter measured on the pre-shot surface

989 d_{rim}: Crater depth from the rim peak to the crater bottom

990 d_{c}: Crater depth from the pre-shot surface to the crater bottom

991 $D_{\mathrm{rim}}/D_{\mathrm{c}}$: Ratio of crater rim diameter to crater diameter

992 $d_{\mathrm{c}}/D_{\mathrm{c}}$: Ratio of crater depth to crater diameter

993 Table 2. Experimental conditions, crater size, and non-dimensional scaling parameters

Run number	Projectile	m_{p}, mg	v_{i}, m s^{-1}	R_{rim}, cm	π_2	π_{R}
140528-1	PC	68.0	2038	7.1	5.60×10^{-9}	15.65
140528-2	PC	68.0	2289	7.6	4.44×10^{-9}	16.86
140528-3	PC	68.0	2500	7.5	3.72×10^{-9}	16.63
140528-4	PC	68.0	3852	8.3	1.57×10^{-9}	18.20
140529-1	PC	68.0	1424	6.5	1.15×10^{-8}	14.37
140529-2	PC	68.0	1552	6.7	9.66×10^{-9}	14.70
140529-3	PC	68.0	1684	6.6	8.21×10^{-9}	14.65
140529-4	PC	68.0	1579	6.4	9.34×10^{-9}	14.16
140530-1	PC	68.0	2279	7.2	4.48×10^{-9}	15.88
140530-2	PC	68.0	3748	8.3	1.66×10^{-9}	18.19
140530-3	PC	68.0	5155	9.6	8.76×10^{-10}	21.08
140530-4	PC	68.0	3381	8.5	2.04×10^{-9}	18.82
140710-2	PC	68.0	221	3.0	4.76×10^{-7}	6.54
140710-6	PC	68.0	170	2.7	8.04×10^{-7}	5.97
140715-2	PC	68.0	222	3.2	4.71×10^{-7}	6.99
140715-3	PC	68.0	217	3.2	4.92×10^{-7}	7.00
140718-1	PC	68.0	227	3.2	4.50×10^{-7}	7.15
140718-2	PC	68.0	208	3.1	5.36×10^{-7}	6.89
140718-3	PC	68.0	204	3.2	5.59×10^{-7}	7.08
140718-4	PC	68.0	217	3.3	4.92×10^{-7}	7.31

140720-1	PC	68.0	173	2.9	7.78×10^{-7}	6.45
140720-2	PC	68.0	211	3.2	5.23×10^{-7}	7.07
140720-3	PC	68.0	217	3.3	4.97×10^{-7}	7.24
140720-4	PC	68.0	189	3.0	6.49×10^{-7}	6.58
140720-5	PC	68.0	205	3.1	5.52×10^{-7}	6.75
141001-1	PC	68.0	1739	6.6	7.70×10^{-9}	14.65
141002-1	PC	68.0	1506	6.5	1.03×10^{-8}	14.32
141002-2	PC	68.0	2495	7.6	3.74×10^{-9}	16.80
141002-3	PC	68.0	3268	8.7	2.18×10^{-9}	19.08
141002-4	PC	68.0	4417	9.3	1.19×10^{-9}	20.51
141002-5	PC	68.0	5754	10.3	7.03×10^{-10}	22.76
141003-1	PC	68.0	6711	11.1	5.17×10^{-10}	24.52
141003-2	PC	68.0	6887	11.4	4.91×10^{-10}	25.19
141003-3	PC	68.0	4003	9.5	1.45×10^{-9}	21.00
141003-4	PC	68.0	1689	6.8	8.16×10^{-9}	14.97
141003-5	PC	68.0	3016	8.4	2.56×10^{-9}	18.62
141202-1	PC	68.0	6158	10.8	6.14×10^{-10}	23.75
141202-2	PC	68.0	6596	10.8	5.35×10^{-10}	23.73
141202-3	PC	68.0	6402	10.9	5.68×10^{-10}	24.08
141203-1	PC	68.0	5192	10.3	8.63×10^{-10}	22.60
141203-2	PC	68.0	5330	9.9	8.19×10^{-10}	21.85
141203-3	PC	68.0	2385	7.5	4.09×10^{-9}	16.62
141203-4	PC	68.0	2254	7.6	4.58×10^{-9}	16.66

141204-1	PC	68.0	2317	7.3	4.34×10^{-9}	16.16
150819-1	PC	68.0	4322	9.7	1.25×10^{-9}	21.33
*150819-3	PC	68.0	4230	8.9	1.30×10^{-9}	19.52
*151104-1	PC	68.0	2208	6.9	4.77×10^{-9}	15.17
*151104-2	PC	68.0	6150	10.1	6.15×10^{-10}	22.29
*151104-3	PC	68.0	1125	5.6	1.84×10^{-8}	12.32
151105-2	PC	68.0	1206	5.8	1.60×10^{-8}	12.87
#150309-1	Al	11.6	4124	5.6	5.76×10^{-10}	22.14
#150310-1	Al	11.6	2077	4.4	2.27×10^{-9}	17.62
#150310-2	Al	11.6	2059	4.5	2.31×10^{-9}	17.67
#150610-1	Al	11.6	1994	4.2	2.46×10^{-9}	16.52
150611-2	Al	11.7	4936	6.1	4.02×10^{-10}	24.14
150611-3	Al	11.7	5015	6.3	3.90×10^{-10}	24.88
#150612-1	Al	11.9	1815	4.0	2.97×10^{-9}	15.70
#150612-2	Al	11.5	2062	4.4	2.30×10^{-9}	17.60
150820-1	Al	11.7	2920	4.7	1.15×10^{-9}	18.77
#150820-7	Al	11.8	3953	5.4	6.27×10^{-10}	21.43
*, #151105-3	Al	11.7	4143	5.3	5.71×10^{-10}	20.94
160721-2	Al	11.9	5622	6.1	3.10×10^{-10}	24.11
150611-5	Gl	10.6	5318	5.8	3.47×10^{-10}	23.93
150611-6	Gl	10.6	2281	4.4	1.88×10^{-9}	18.19
#150612-5	Gl	11.3	2023	4.2	2.39×10^{-9}	16.86
*, #150820-2	Gl	10.9	4023	5.2	6.06×10^{-10}	21.24

150821-1	Gl	10.7	3427	5.1	8.34×10^{-10}	20.77
#150821-2	Gl	10.6	4013	5.3	6.09×10^{-10}	21.58
#150311-1	Ti	18.9	4097	6.5	5.84×10^{-10}	22.00
*,#150820-3	Ti	18.9	3834	5.9	6.67×10^{-10}	20.06
#150821-3	Ti	18.8	2044	5.1	2.35×10^{-9}	17.37
#150821-4	Ti	18.8	1972	5.0	2.52×10^{-9}	16.84
160720-1	Ti	18.8	5181	6.7	3.65×10^{-10}	22.68
#150309-3	ZrO_2	26.5	3864	6.9	6.56×10^{-10}	20.79
#150311-7	ZrO_2	25.7	2004	5.7	2.44×10^{-9}	17.31
*,#150820-4	ZrO_2	25.4	3934	6.7	6.33×10^{-10}	20.42
#160719-3	ZrO_2	26.9	2153	5.4	2.11×10^{-9}	16.26
160720-2	ZrO_2	24.2	5727	7.3	2.99×10^{-10}	22.85
#150309-2	SUS	32.4	3943	7.5	6.30×10^{-10}	21.14
#150310-3	SUS	32.6	2018	5.7	2.41×10^{-9}	16.01
#150610-2	SUS	32.6	1841	5.7	2.89×10^{-9}	16.12
150611-4	SUS	32.6	4936	8.4	4.02×10^{-10}	23.55
#150612-3	SUS	32.6	1848	5.7	2.87×10^{-9}	15.98
#150612-4	SUS	32.8	1824	5.8	2.95×10^{-9}	16.18
*,#150820-6	SUS	32.6	3805	7.1	6.77×10^{-10}	20.07
#150310-6	Cu	37.8	3962	7.6	6.24×10^{-10}	20.32
*150820-5	Cu	38.1	3626	7.2	7.45×10^{-10}	19.33
#151105-1	Cu	37.8	2114	6.0	2.19×10^{-9}	16.01
160719-1	Cu	38.2	2238	6.2	1.96×10^{-9}	16.60

160720-4	Cu	37.9	5348	7.9	3.43×10^{-10}	21.10
160721-3	Cu	37.9	2306	6.3	1.84×10^{-9}	16.75
150309-4	WC	62.1	3726	9.1	7.06×10^{-10}	20.63
150312-2	WC	61.9	1786	6.8	3.07×10^{-9}	15.47
*150819-4	WC	62.5	3422	8.3	8.37×10^{-10}	18.82

994 The asterisk (*) indicates the example of the crater profile shown on Fig. 3.

995 The sharp (#) indicates the data calculating by Eq. (5) shown on Fig. 5.

996 m_{p}: projectile mass

997 v_{i}: impact velocity

998 R_{rim}: crater rim radius

999 π_2: a scaling parameter defined by Eq. (2)

1000 π_{R}: a scaling parameter defined by Eq. (1)

1001 Table 3. Experimental conditions and results of a PC projectile at low impact velocity.

Run number	v_i, m s^{-1}	E_k, J	R_rim, cm	x, cm	x/R_rim	t_max, ms	g_max, m s^{-2}	T_half, ms
140710-2	221	1.7	3.0	5.1	1.6	0.42	30.0	1.13
				7.5	2.5	0.87	7.1	0.63
140715-2	222	1.67	3.2	6.0	1.8	0.39	35.5	0.79
140718-2	208	1.5	3.1	5.7	1.7	0.87	18.1	1.52
				6.6	2.0	0.70	12.4	1.02
				7.2	2.2	1.01	6.75	1.66
140718-3	204	1.4	3.2	8.8	2.7	1.32	7.13	1.59
140718-4	217	1.6	3.3	9.4	2.8	1.31	9.6	0.78
140720-1	173	1.0	2.9	6.4	2.1	0.66	10.5	1.02

1002 v_i: Impact velocity

1003 E_k: Kinetic energy of the projectile

1004 R_rim: Crater rim radius

1005 x: Distance from the impact point to the accelerometer

1006 t_max: Traveling time from the impact time to the time when the acceleration becomes the maximum

1007 g_max: Maximum acceleration

1008 T_half, Duration of the first upward acceleration

1009 Table 4. Experimental conditions and results of a PC projectile at high impact velocity.

Run number	v_i, m s^{-1}	E_k, J	R_{rim}, cm	x, cm	x/R_{rim}	t_{max}, ms	g_{max}, m s^{-2}	T_{half}, ms
140530-1	2279	176.6	7.6	10.3	1.4	0.93	67.3	1.25
				16.2	2.1	1.74	17.0	1.44
				25.1	3.3	3.07	2.8	1.66
140530-2	3748	477.6	8.7	12.3	1.4	0.94	116.4	1.02
				17.2	2.0	1.83	27.6	1.90
				25.1	2.9	2.81	8.2	1.50
140530-3	5155	903.5	10.2	15.2	1.5	1.26	116.2	1.24
				20.2	2.0	2.03	22.0	1.28
				27.1	2.7	3.49	15.3	2.33
140530-4	3381	388.7	8.9	15.2	1.7	1.64	57.2	0.89
				20.2	2.3	2.41	21.9	1.55
				30.1	3.4	3.59	9.7	1.32
141001-1	1739	102.8	6.6	10.7	1.6	0.97	45.6	1.77
				14.0	2.1	1.56	25.1	1.64
141002-1	1506	77.1	6.5	8.9	1.4	–	35.0	1.17
				12.0	1.9	–	30.7	1.81
				15.2	2.3	–	9.7	1.52
141002-2	2495	211.7	7.6	12.1	1.6	1.05	56.9	2.48
				14.8	1.9	1.72	30.1	2.46
141002-3	3268	363.1	8.6	18.9	2.2	2.30	28.4	2.04

141002-4	4417	663.3	9.3	16.6	1.8	1.77	44.0	2.53
				20.6	2.2	2.56	13.9	2.57
141002-5	5754	1125.7	10.3	15.4	1.5	1.58	69.5	1.94
				20.2	2.0	2.38	13.8	1.68
141003-1	6711	1531.3	11.1	15.0	1.3	1.27	77.7	2.46
				20.6	1.9	2.16	34.3	2.66
141003-2	6887	1612.7	11.4	13.3	1.2	0.97	118.2	1.23
				17.2	1.5	1.59	79.7	2.05
				23.8	2.1	3.10	21.6	2.24
141003-3	4003	544.8	9.5	13.6	1.4	1.25	63.7	1.87
				17.6	1.8	2.10	25.6	1.88
				23.6	2.5	3.09	5.6	2.28
141003-4	1689	97.0	6.8	7.9	1.2	0.42	46.4	1.78
				15.3	2.2	1.99	28.9	2.10
				23.1	3.4	3.07	5.6	2.18
141003-5	3016	309.3	8.4	10.1	1.2	0.81	53.0	1.75
				15.7	1.9	2.12	28.8	2.09
				19.9	2.4	2.98	11.4	2.48
141202-1	6158	1289.3	10.8	20.1	1.9	1.97	30.0	1.94
				23.1	2.1	2.42	14.2	2.15
141202-2	6596	1479.3	10.8	15.3	1.4	1.67	47.8	2.61
				17.6	1.6	1.97	34.5	2.60

				24.6	2.3	3.59	14.2	2.40
141202-3	6402	1393.5	10.9	14.6	1.3	1.85	35.9	2.27
				19.8	1.8	2.46	33.5	2.16
				24.2	2.2	3.78	15.7	2.15
141203-1	5192	916.5	10.2	14.3	1.4	1.84	53.5	1.99
				17.1	1.7	2.12	27.9	2.04
				23.4	2.3	3.51	16.1	1.55
141203-2	5330	965.9	9.9	12.1	1.2	1.13	77.8	2.17
				16.7	1.7	2.20	26.0	2.52
				19.6	2.0	2.91	20.9	2.29
				19.9	2.0	2.91	10.5	2.60
150819-1	4322	635.1	9.7	11.6	1.2	0.88	86.6	1.91
				17.8	1.8	2.03	27.6	1.95
				23.6	2.4	2.88	14.8	1.78
				26.0	2.7	3.38	9.1	1.61
150819-3	4230	608.4	8.9	12.9	1.5	1.27	68.0	2.13
				15.7	1.8	1.86	36.0	2.28
				20.6	2.3	2.62	19.7	2.44
				26.2	3.0	3.75	11.2	2.21
151104-1	2208	165.8	6.9	12.4	1.8	1.51	47.3	1.48
				13.9	2.0	1.89	27.3	1.89
				15.2	2.2	2.24	19.3	1.52

				19.2	2.8	2.74	9.7	1.58
				23.3	3.4	3.27	3.7	2.14
151104-3	1125	43.0	5.6	12.1	2.2	1.53	7.9	1.66
				15.6	2.8	2.13	3.6	2.66
				19.2	3.4	2.78	2.8	1.97
151105-2	1206	49.5	5.8	10.3	1.8	0.96	6.9	2.94
				13.0	2.2	1.48	6.5	2.05
				16.5	2.8	2.13	5.3	1.72
				18.3	3.1	2.52	5.2	1.74
				21.5	3.7	3.06	4.0	1.54

1010

1011 Table 5. Experimental conditions and results of 2-mm projectiles with different densities.

Run number	Projectile	v_i, m s^{-1}	E_k, J	R_{rim}, cm	x, cm	x/R_{rim}	t_{max}, ms	g_{max}, m s^{-2}	T_{half}, ms
150611-5	Gl	5318	150.3	5.8	11.1	1.9	1.45	14.7	2.39
					15.1	2.6	2.29	5.6	2.19
					21.0	3.6	3.42	1.5	2.07
					23.0	3.9	3.36	1.6	1.82
150611-6	Gl	2281	28.0	4.4	13.1	3.0	2.16	3.1	2.12
					18.2	4.1	2.37	0.5	1.49
					23.3	5.2	3.59	0.5	1.77
					23.9	5.4	4.17	0.4	1.58
150612-5	Gl	2023	23.1	4.2	9.2	2.2	1.45	8.9	2.13
					17.3	4.1	2.39	0.5	1.11
150820-2	Gl	4023	88.2	5.0	14.1	2.8	2.07	7.1	2.10
					17.9	3.6	2.77	5.0	1.94
					21.9	4.4	3.43	2.4	1.85
150821-1	Gl	3427	62.5	5.0	14.2	2.8	1.96	5.0	1.96
					16.2	3.2	2.49	5.1	1.93
					23.2	4.6	3.58	0.9	1.87
150821-2	Gl	4013	85.5	5.1	13.2	2.6	1.93	7.4	2.81
					16.7	3.3	2.66	4.0	2.29
					20.4	4.0	3.33	2.3	2.15
150309-1	Al	4124	98.8	5.7	9.6	1.7	0.99	36.2	1.82

					12.7	2.2	1.97	12.4	1.40
					12.8	2.2	1.49	11.1	1.18
					14.8	2.6	2.01	8.0	1.13
					19.3	3.4	2.48	5.4	1.29
150310-2	Al	2059	24.7	4.4	10.6	2.4	1.86	7.9	1.40
					21.9	4.9	3.85	0.9	1.60
150610-1	Al	1994	23.1	4.2	7.9	1.9	0.86	12.7	0.99
					9.9	2.4	1.13	11.3	1.07
					13.9	3.3	1.87	3.8	1.36
					17.3	4.2	2.16	2.5	1.45
					24.2	5.8	3.61	1.4	1.42
150611-2	Al	4936	142.3	6.1	13.2	2.2	1.78	7.5	1.88
					17.7	2.9	2.49	4.1	1.74
					20.1	3.3	2.65	2.1	1.81
					25.6	4.2	3.48	1.1	1.64
150611-3	Al	5015	146.9	6.3	13.5	2.2	1.70	8.2	1.72
					18.3	2.9	2.53	4.2	1.25
					20.5	3.3	2.72	3.1	1.54
150612-1	Al	1815	19.6	4.0	16.0	4.0	2.25	1.5	1.40
					22.2	5.6	3.00	0.7	1.33
150612-2	Al	2062	24.5	4.4	21.9	5.0	2.69	0.3	1.52
150820-1	Al	2920	49.9	4.6	12.0	2.6	1.33	14.5	1.83
					15.3	3.3	1.92	5.8	1.66

					18.5	4.0	2.68	5.6	1.79
150820-7	Al	3953	92.0	5.2	12.2	2.3	1.76	8.0	1.88
					17.5	3.3	2.68	2.7	2.14
151105-3	Al	4143	100.3	5.4	10.7	2.0	1.30	13.6	2.34
					13.0	2.4	2.01	6.2	1.72
					15.4	2.8	2.46	3.5	1.68
					18.1	3.3	2.82	3.8	1.73
					22.4	4.1	3.33	2.6	1.53
150311-1	Ti	4097	159.0	6.5	13.4	2.1	1.88	10.7	2.38
					15.9	2.4	2.32	5.1	2.51
					18.1	2.8	2.84	6.5	2.08
					20.5	3.1	3.50	1.8	1.66
150820-3	Ti	3834	138.8	5.8	12.1	2.1	–	16.5	2.53
					18.4	3.2	–	9.8	2.06
					24.6	4.2	–	3.5	1.73
150821-5	Ti	1972	36.6	4.8	14.0	2.9	2.04	4.0	1.48
					15.1	3.2	2.39	4.1	1.92
					19.8	4.2	3.22	1.8	1.89
150309-3	ZrO_2	3864	197.8	6.9	10.0	1.4	0.94	24.0	2.43
					15.3	2.2	2.21	15.8	2.31
					18.2	2.6	2.67	4.4	2.03
					19.1	2.8	2.82	6.2	1.82
					22.6	3.3	3.61	3.2	1.67

150311-7	ZrO_2	2004	51.5	5.7	12.5	2.2	1.83	12.7	1.80
150820-4	ZrO_2	3934	196.5	6.6	11.7	1.8	1.23	15.4	2.76
					15.0	2.3	1.94	7.5	2.53
					17.2	2.6	2.51	12.2	2.09
					22.1	3.3	3.21	5.3	1.77
150309-2	SUS	3943	252.1	7.5	14.9	2.0	2.36	12.9	2.28
					16.4	2.2	2.73	8.7	2.43
					17.7	2.4	2.67	8.8	2.06
					21.1	2.8	3.56	3.5	1.98
150310-3	SUS	2018	66.4	5.7	17.4	3.1	3.19	3.3	2.10
150610-2	SUS	1841	55.2	5.7	11.6	2.0	1.78	11.7	1.87
					15.9	2.8	2.53	3.3	2.05
					21.2	3.7	3.10	1.2	1.60
					25.3	4.4	3.80	1.1	1.71
150611-4	SUS	4936	397.5	8.4	15.6	1.9	1.85	14.9	2.21
					18.1	2.2	2.77	7.7	2.09
					21.6	2.6	3.32	4.6	2.52
					24.8	3.0	3.92	7.6	2.28
150612-3	SUS	1848	55.6	5.7	15.6	2.7	2.25	6.6	1.94
					21.6	3.8	3.27	2.0	1.82
150612-4	SUS	1824	54.5	5.8	11.8	2.1	1.64	9.1	1.95
150820-6	SUS	3805	235.6	7.0	12.7	1.8	1.44	26.0	2.71
					17.3	2.5	2.49	22.1	2.17

					21.0	3.0	3.25	8.2	1.82
					24.0	3.4	3.51	6.5	1.55
150310-6	Cu	3962	296.4	7.6	14.8	2.0	1.98	15.4	2.00
					17.1	2.3	2.55	14.1	2.36
					20.0	2.6	2.88	7.7	2.00
					23.4	3.1	3.61	6.0	1.50
150820-5	Cu	3626	250.1	7.1	13.9	2.0	1.45	20.0	2.20
					18.4	2.6	2.76	14.2	1.96
					25.0	3.5	3.38	7.5	1.67
151105-1	Cu	2114	84.5	6.0	9.9	1.6	0.87	28.5	1.09
					14.1	2.3	1.54	10.0	1.49
					17.2	2.9	2.31	5.8	1.15
					19.7	3.3	2.75	7.1	1.20
					24.8	4.1	3.41	3.1	1.44
150309-4	WC	3726	430.7	9.1	14.0	1.5	1.42	40.9	2.06
					15.8	1.7	1.87	37.0	1.99
					20.6	2.3	2.79	13.0	1.99
					21.2	2.3	2.81	12.9	2.02
					24.4	2.7	3.76	8.4	2.19
150312-2	WC	1786	98.8	6.4	12.2	1.9	2.13	12.4	2.70
					15.8	2.5	3.39	8.5	2.80
150819-4	WC	3422	366.2	8.2	12.7	1.6	1.16	46.3	2.89
					15.6	1.9	1.68	16.5	2.95

					18.5	2.3	2.46	20.8	2.65
					26.2	3.2	3.75	6.8	2.05

1012

1013 Table 6. Propagation velocity, parameters related to maximum acceleration on Eq. (7) for a PC projectile at different impact velocities.

1014

Impact velocity v_{i}, km s^{-1}	Propagation velocity V_{prop}, m s^{-1}	Average crater rim radius $R_{\mathrm{rim\_ave}}$, cm	Eq. (7) related to maximum acceleration g_{max}	
			a_{r}	b_{r}
0.2	37.4 (7.3)	3.1	-1.68 (0.88)	2.38 (0.76)
1	53.4 (2.9)	5.7	-0.18 (0.30)	1.08 (0.36)
1.5	56.4 (3.9)	6.6	-0.35 (0.41)	1.92 (0.46)
2	57.2 (7.1)	7.6	-1.77 (0.16)	3.78 (0.20)
3	65.0 (10.2)	8.9	0.09 (0.37)	1.75 (0.48)
4	56.5 (3.0)	9.0	-0.92 (0.19)	3.14 (0.25)
5	47.9 (8.1)	10.1	-0.46 (0.49)	2.59 (0.66)
6	40.7 (12.9)	10.7	-0.39 (0.60)	2.52 (0.84)
7	45.3 (4.5)	11.1	-0.54 (0.38)	2.93 (0.51)

1015

1016 The number in the parentheses indicates the standard error.

1017 Table 7. Propagation velocity, parameters related to maximum acceleration on Eq. (7) for 2-mm projectiles with different densities.

Projectile	Impact velocity v_{i}, km s^{-1}	Propagation velocity V_{prop}, m s^{-1}	Average crater rim radius $R_{\mathrm{rim\_ave}}$, cm	Eq. (7) related to maximum acceleration g_{max}	
				a_{r}	b_{r}
Al	2	56.1 (7.5)	4.2	-2.08 (0.39)	3.00 (0.48)
	3	47.5 (4.0)	4.6	-0.98 (0.86)	2.27 (1.03)
	4	53.4 (5.6)	5.5	-1.42 (0.38)	2.70 (0.45)
	5	70.6 (3.9)	6.2	-1.56 (0.25)	2.84 (0.33)
Gl	2	54.0 (9.1)	4.3	-2.64 (0.45)	3.41 (0.57)
	3	56.6 (6.7)	5.0	-2.33 (0.77)	3.68 (1.01)
	4	55.0 (3.0)	5.1	-1.21 (0.32)	2.40 (0.41)
	5	56.8 (7.6)	5.8	-1.95 (0.25)	3.26 (0.31)
Ti	2	50.3 (6.0)	4.8	-1.43 (0.43)	2.43 (0.54)
	4	43.0 (3.3)	7.3	-1.01 (0.61)	2.35 (0.78)
ZrO_2	4	48.9 (2.4)	6.8	-0.76 (0.35)	2.15 (0.44)
SUS	2	60.4 (7.7)	5.7	-1.81 (0.28)	3.04 (0.36)
	4	49.8 (7.3)	7.3	-0.81 (0.62)	2.41 (0.83)
	5	45.2 (6.0)	8.4	-0.27 (0.84)	1.66 (1.19)
Cu	2	56.4 (3.8)	6.0	-0.87 (0.26)	2.27 (0.33)
	4	52.4 (7.7)	7.3	-0.34 (0.26)	1.90 (0.35)
WC	3	51.5 (3.1)	8.2	-0.54 (0.51)	2.39 (0.66)
	4	46.1 (2.9)	9.1	-0.96 (0.20)	3.06 (0.27)

1018 The number in the parentheses indic1ates the standard error.

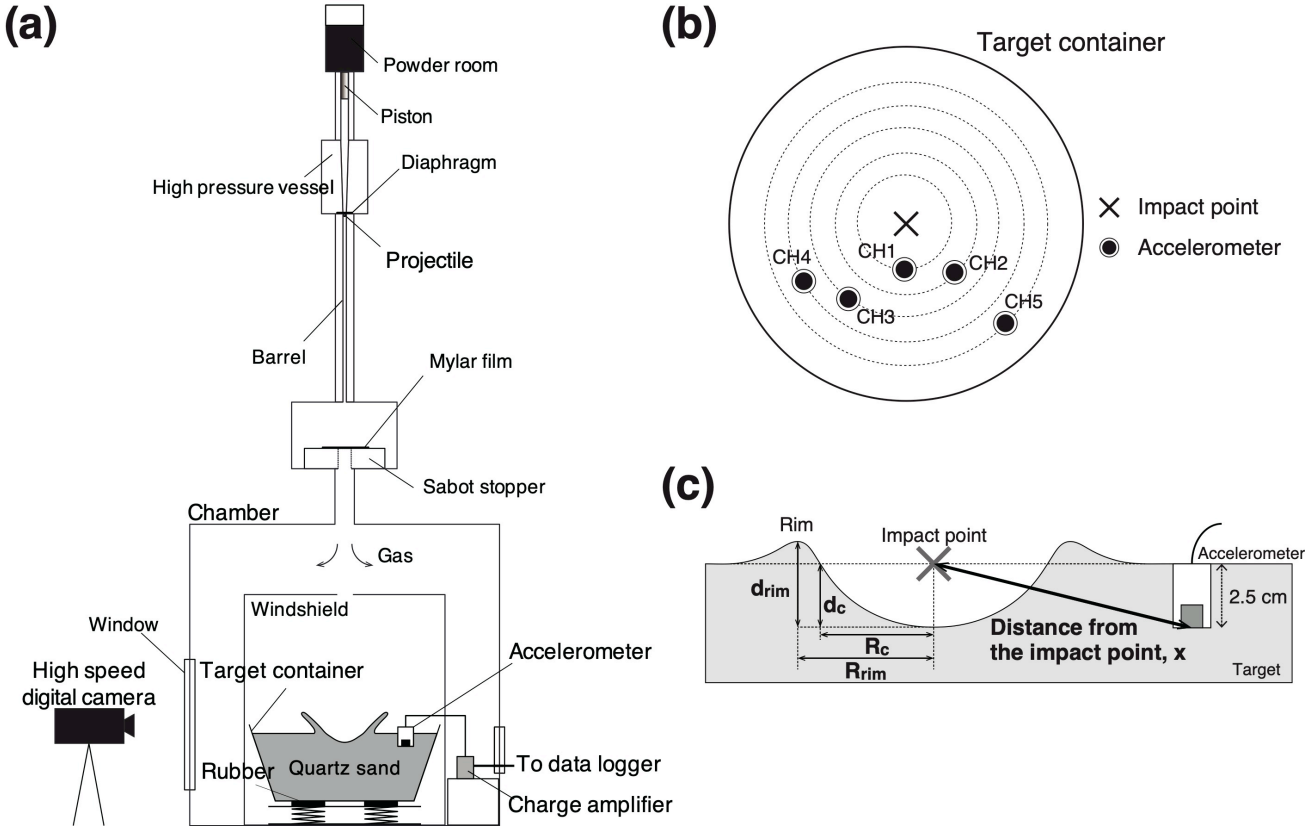

1019

1020 Figure 1

1021 Matsue et al.

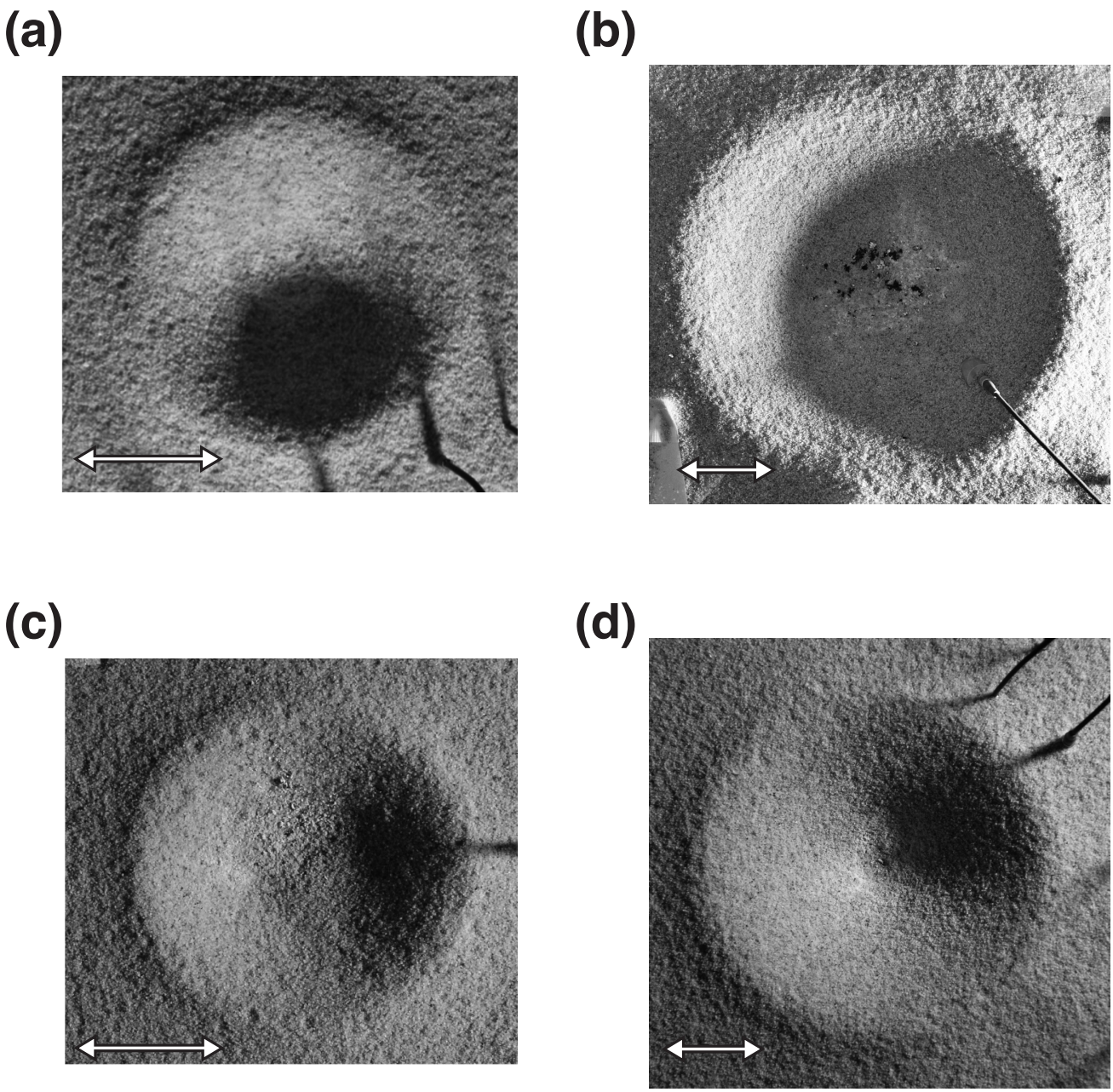

Figure 2

Matsue et al.

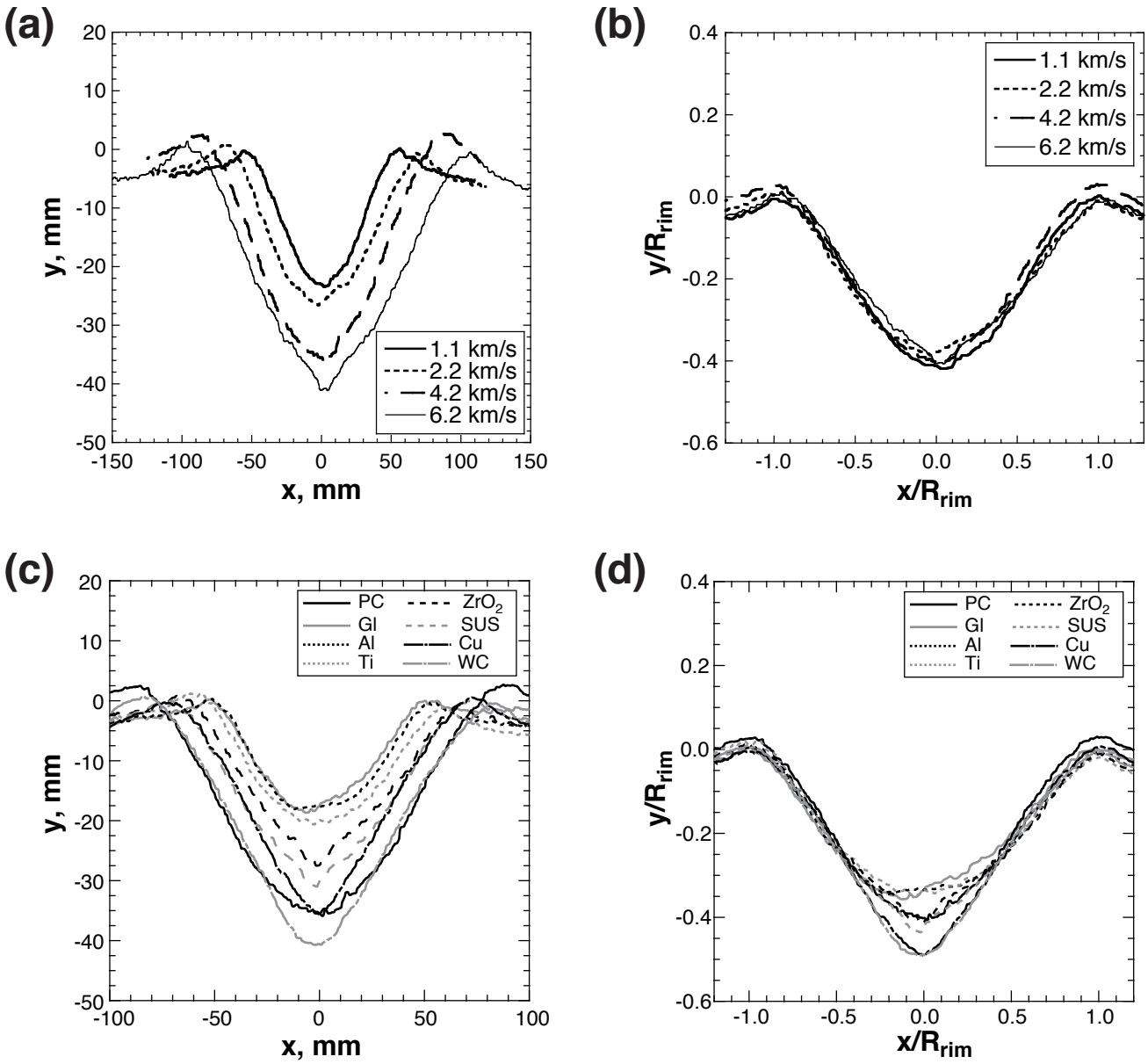

1025

1026 Figure 3

1027 Matsue et al.

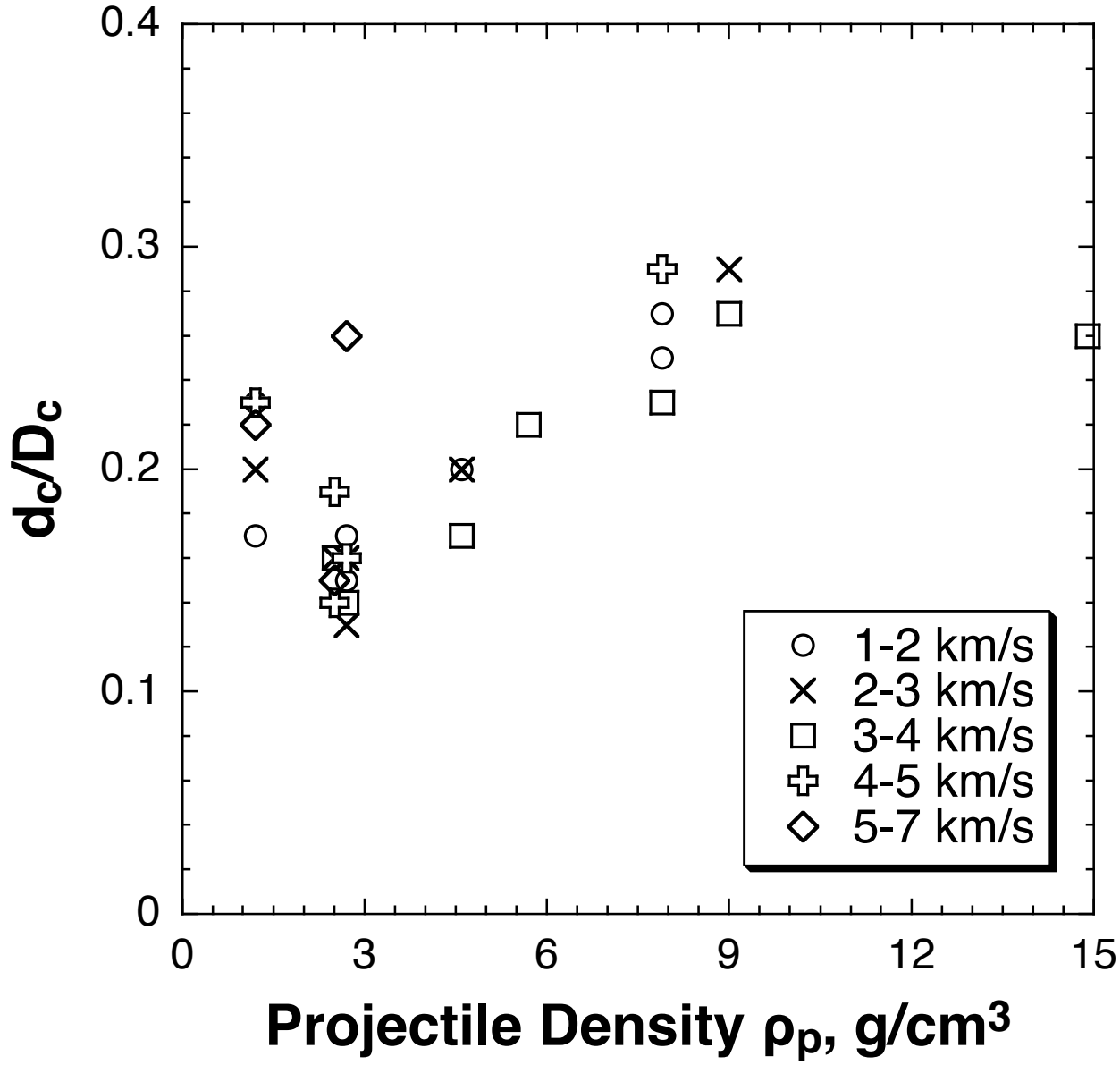

1028

1029 Figure 4

1030 Matsue et al.

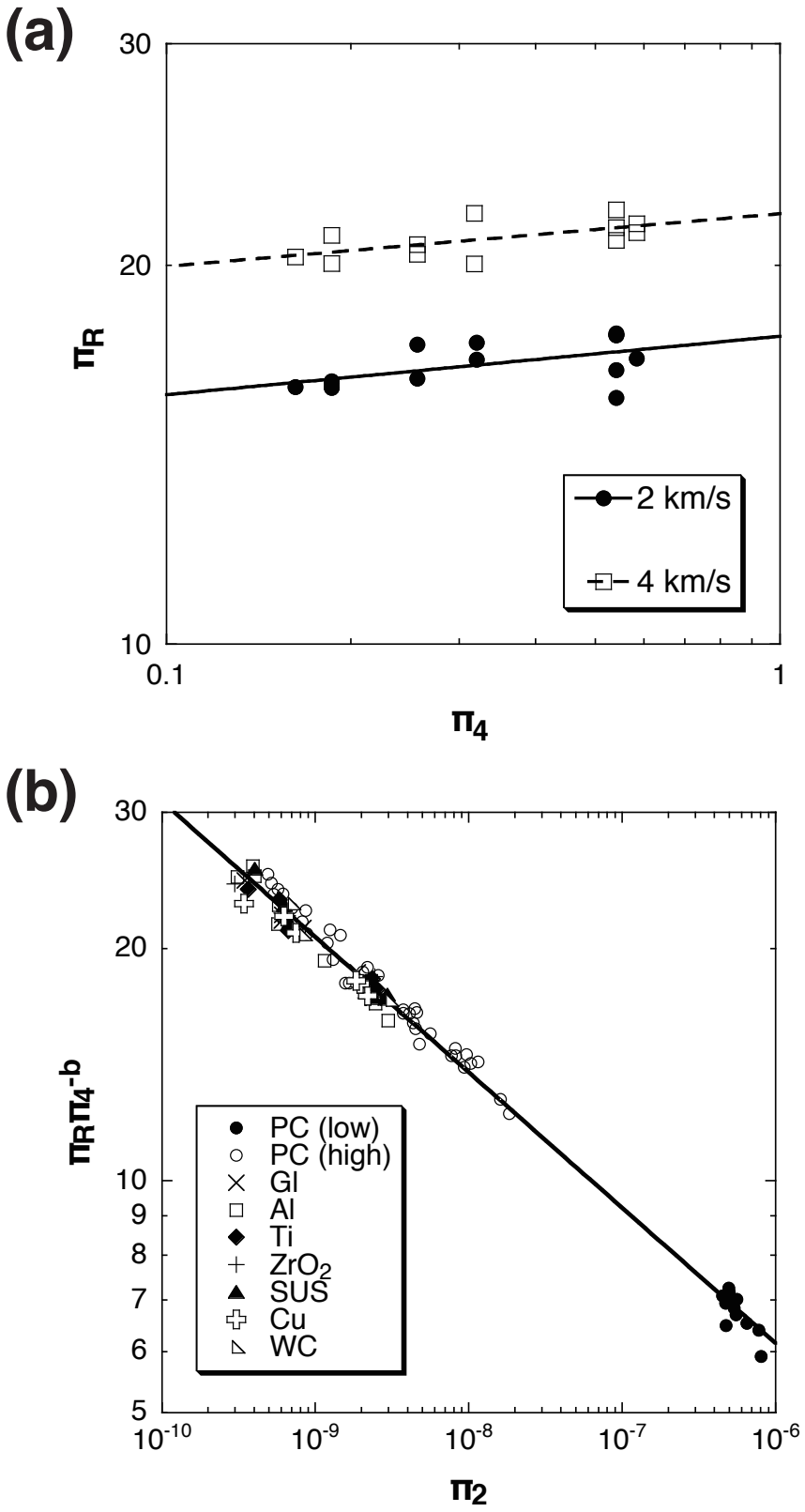

1031

1032 Figure 5

1033 Matsue et al.

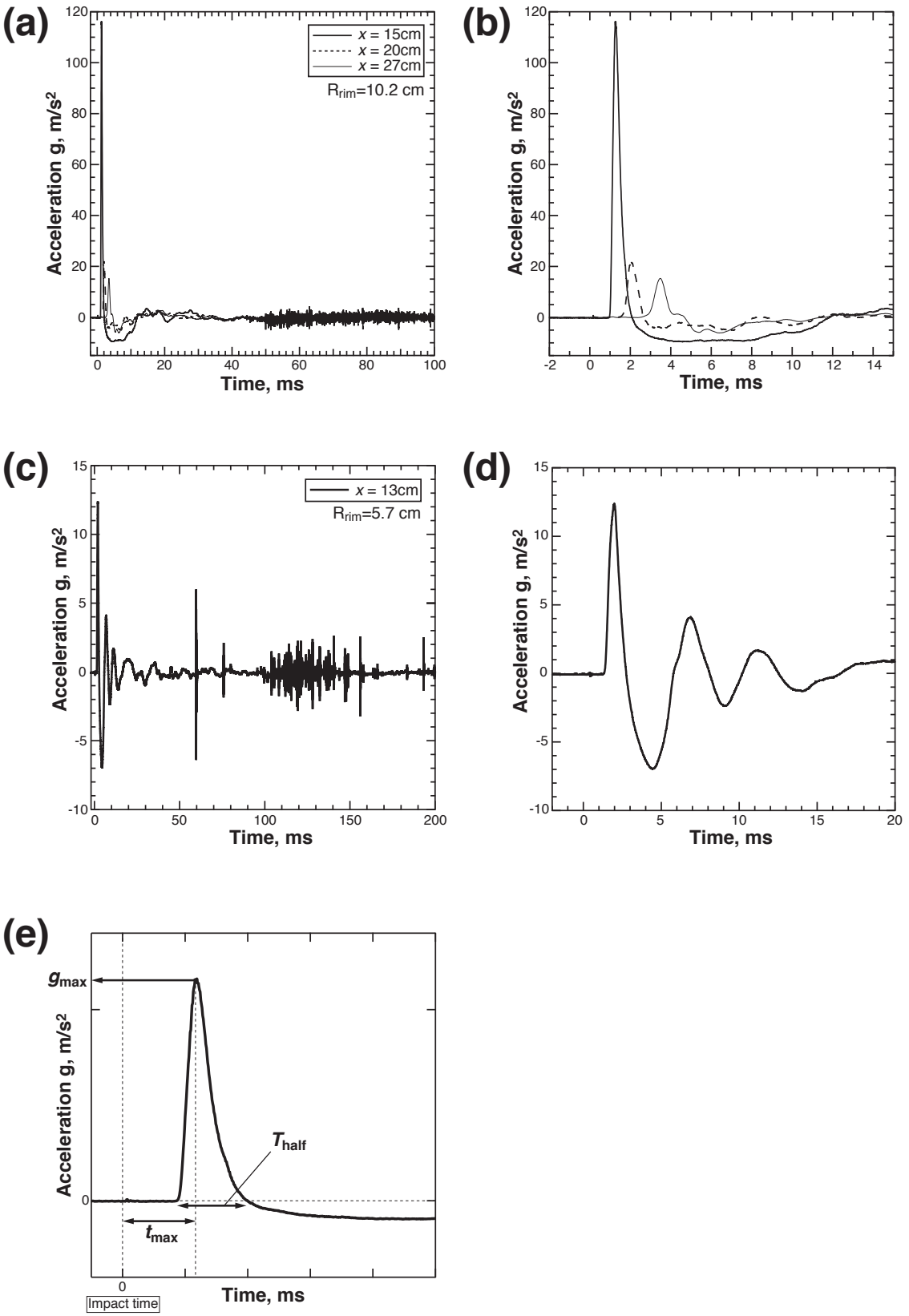
(a)
x = 15cm
x = 20cm
x = 27cm
R_rim=10.2 cm
Acceleration g, m/s²
Time, ms
(b)
Acceleration g, m/s²
Time, ms
(c)
x = 13cm
R_rim=5.7 cm
Acceleration g, m/s²
Time, ms
(d)
Acceleration g, m/s²
Time, ms
(e)
g_max
T_half
t_max
Acceleration g, m/s²
Impact time
Time, ms

Figure 6

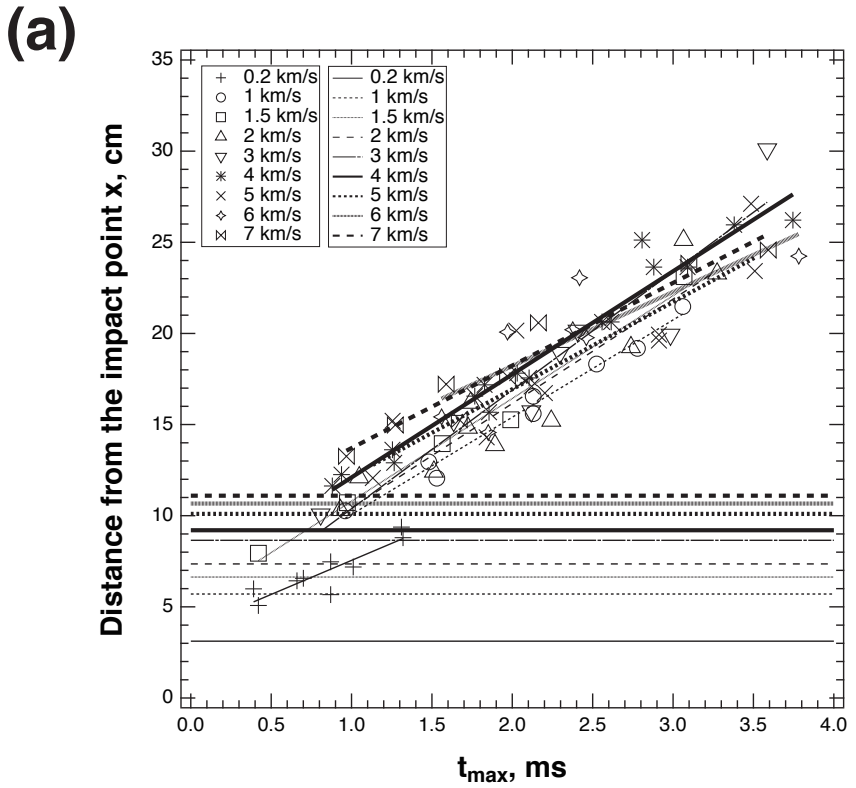

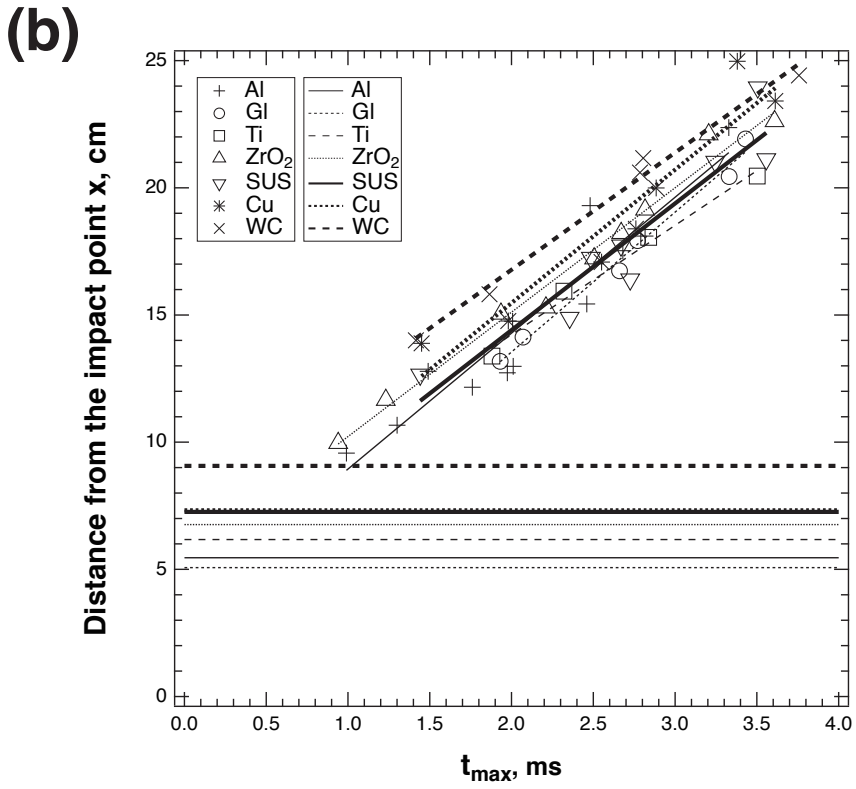

Figure 7

Matsue et al.

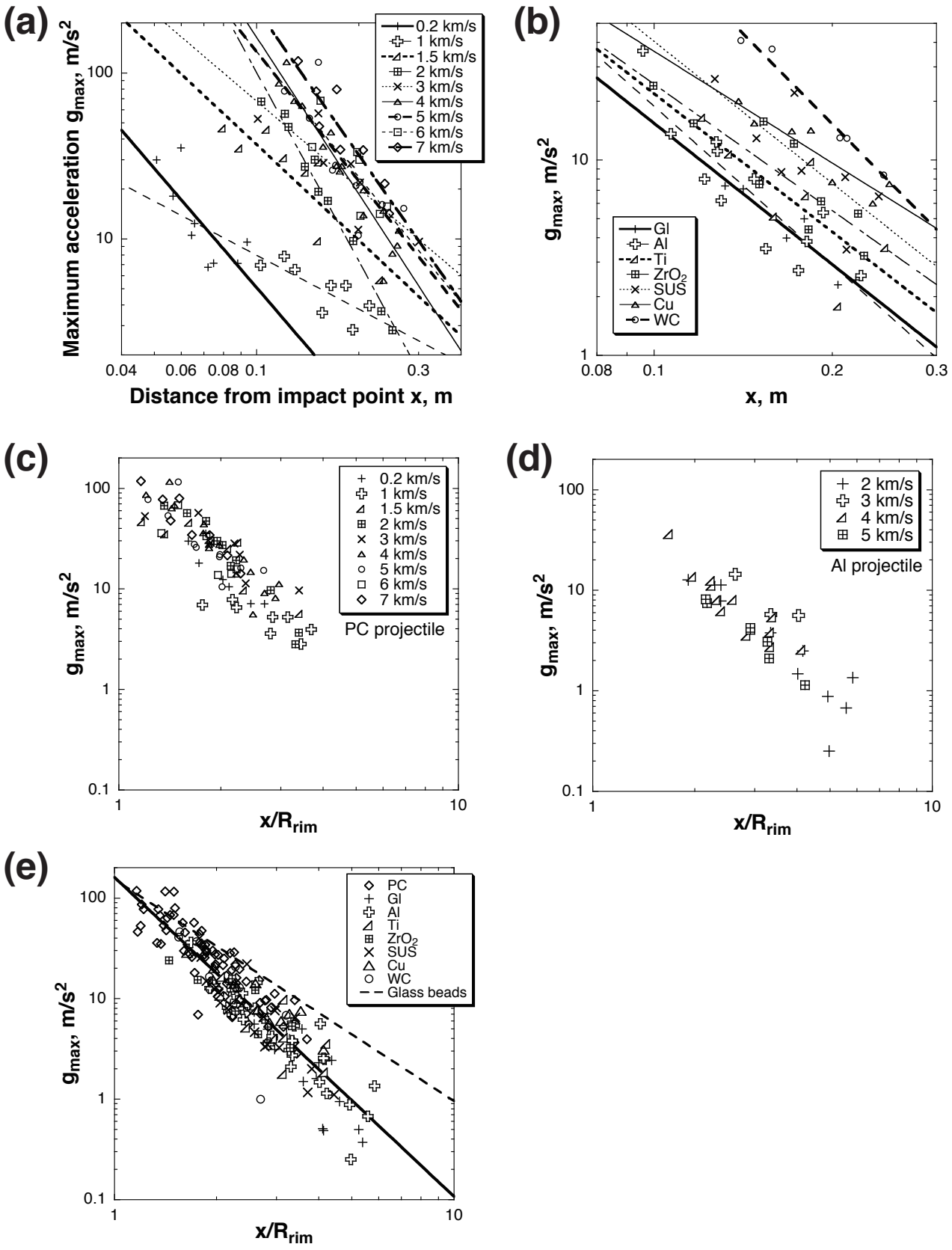
(a)
Maximum acceleration g_{max}, m/s^2
Distance from impact point x, m
0.2 km/s
1 km/s
1.5 km/s
2 km/s
3 km/s
4 km/s
5 km/s
6 km/s
7 km/s
(b)
g_{max}, m/s^2
x, m
Gl
Al
Ti
ZrO_2
SUS
Cu
WC
(c)
g_{max}, m/s^2
x/R_{rim}
PC projectile
(d)
g_{max}, m/s^2
x/R_{rim}
Al projectile
(e)
g_{max}, m/s^2
x/R_{rim}
PC
Gl
Al
Ti
ZrO_2
SUS
Cu
WC
Glass beads

Figure 8

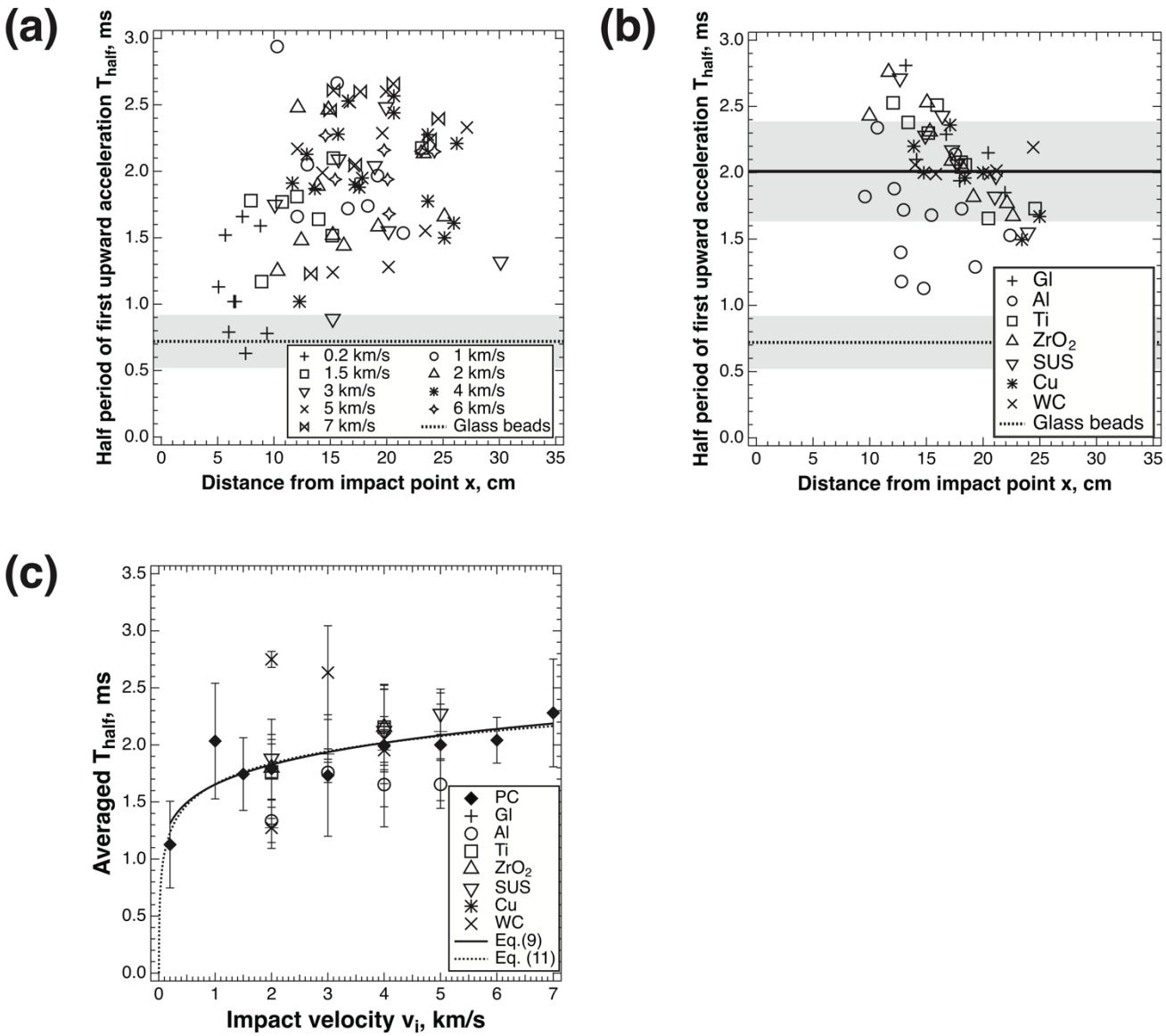

1044

1045 Figure 9

1046 Matsue et al.

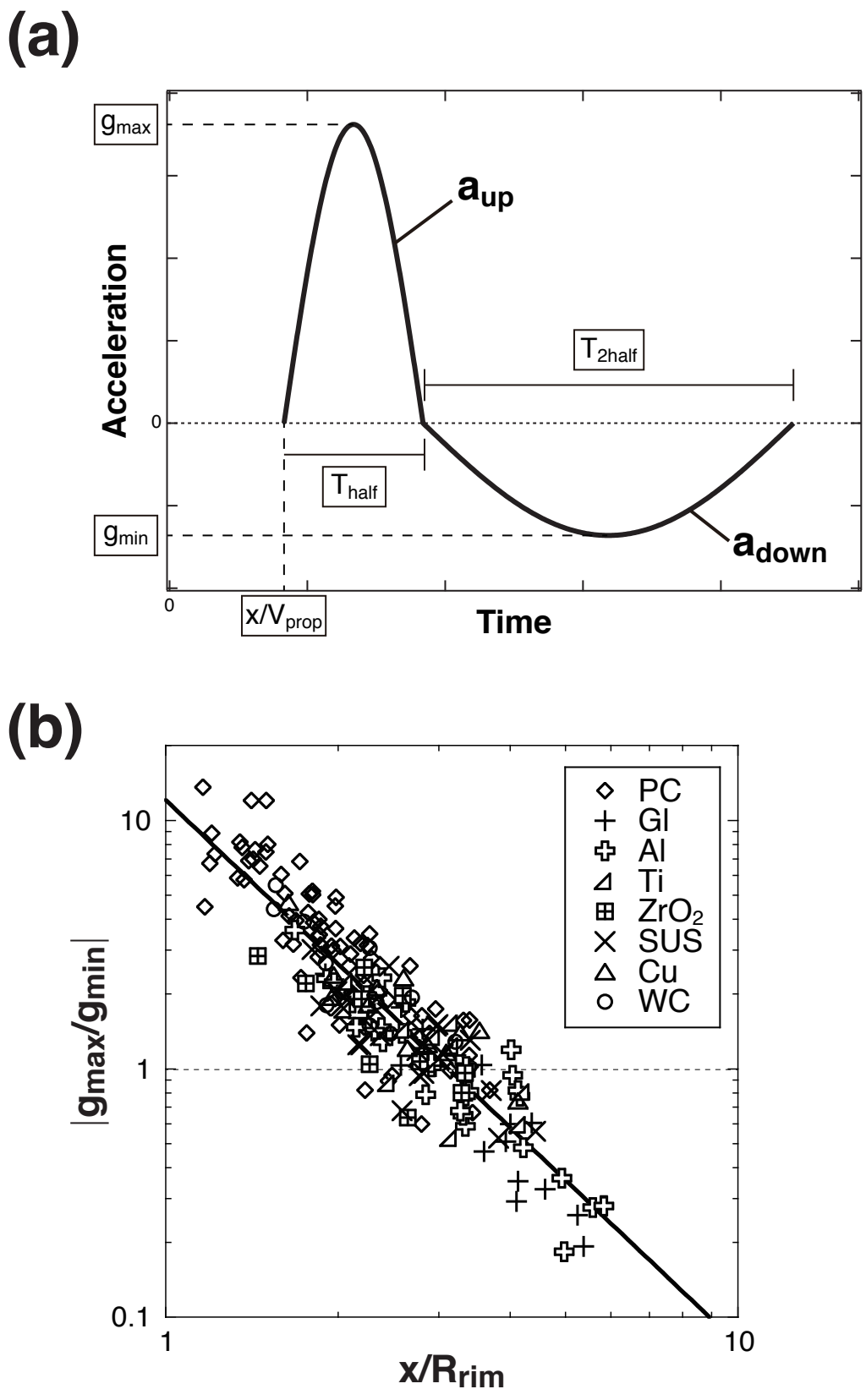

1047

1048 Figure 10

1049 Matsue et al.

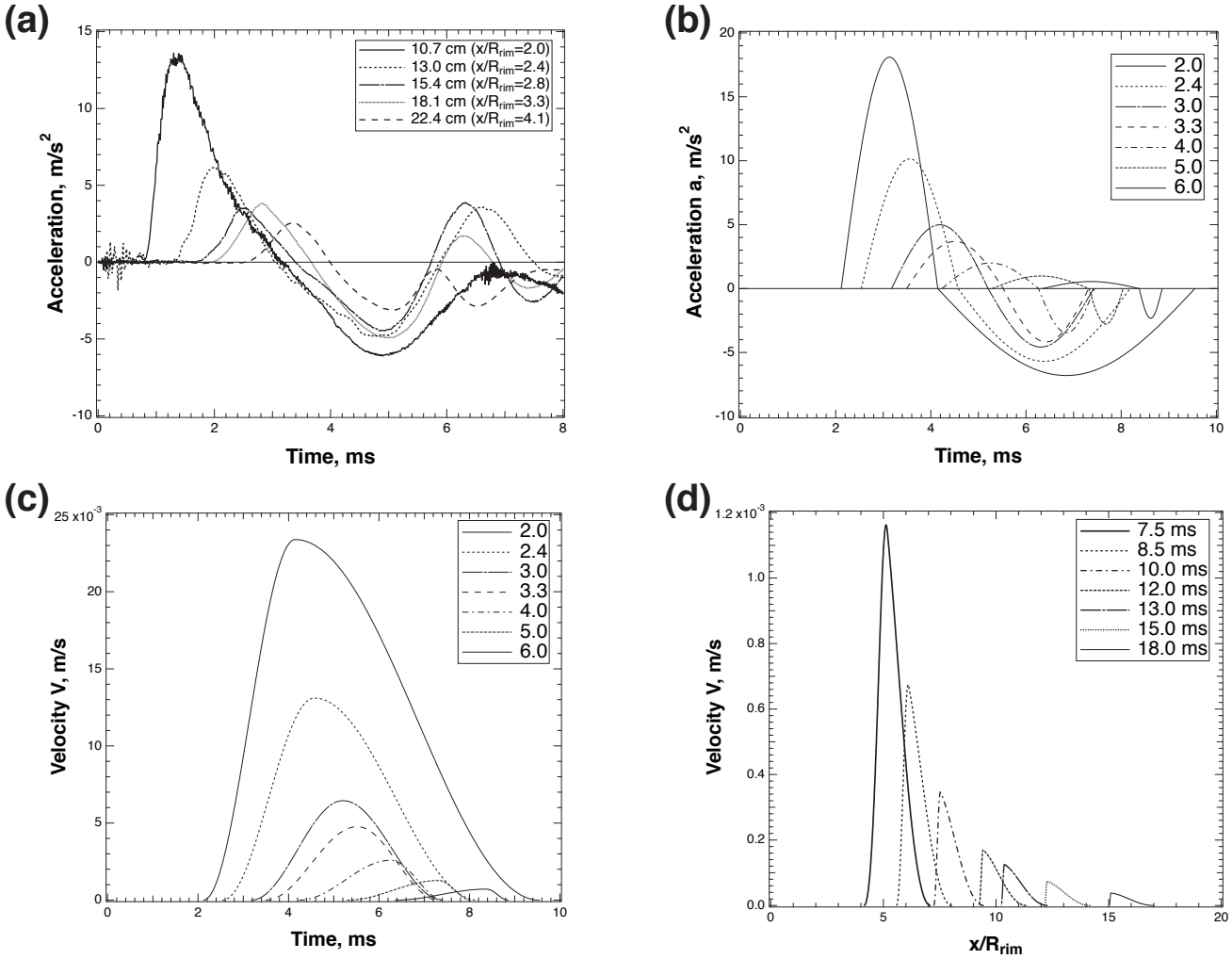

1050

1051 Figure 11

1052 Matsue et al.

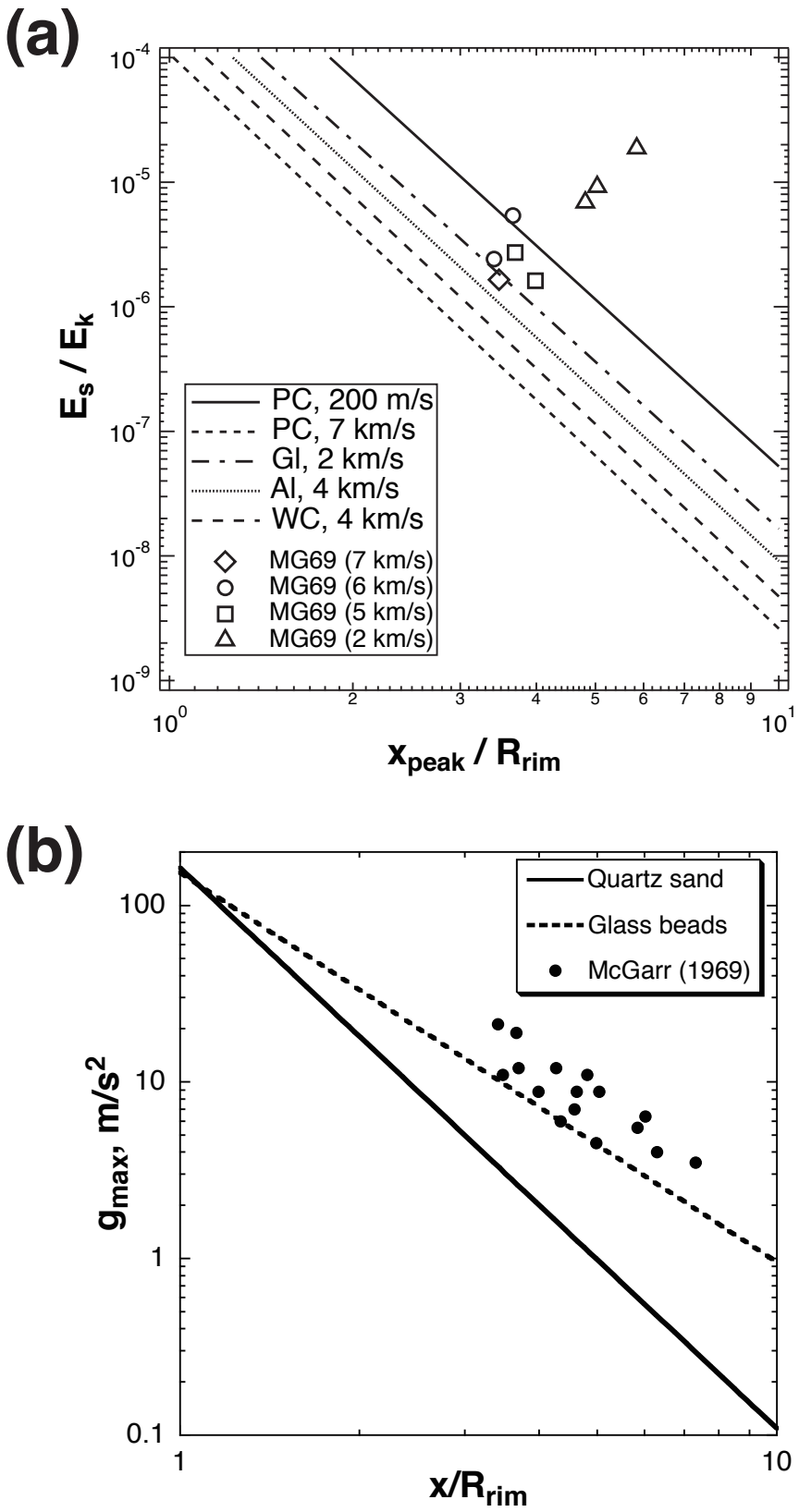

Figure 12

Matsue et al.

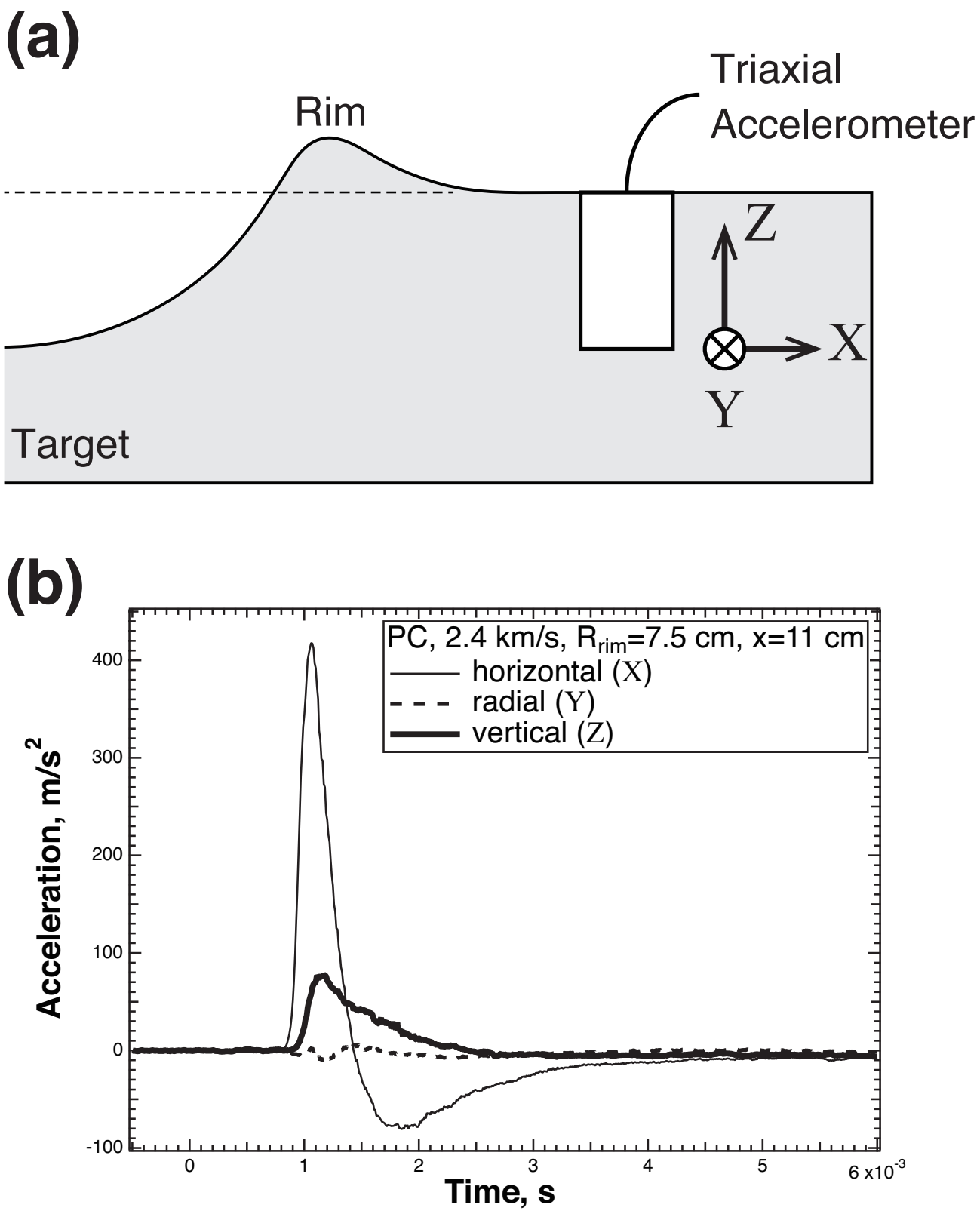

1056

1057 Figure 13

1058 Matsue et al.

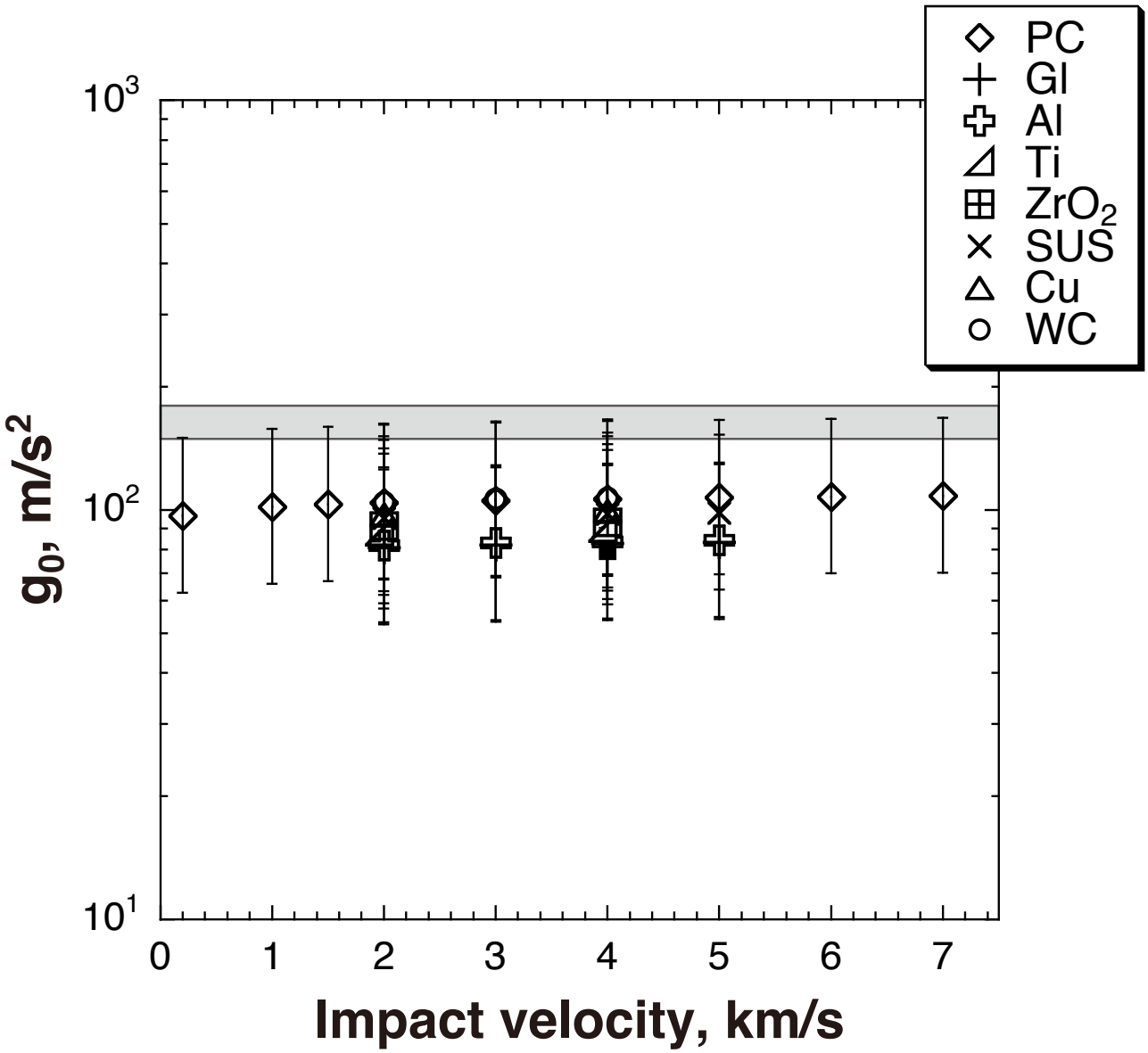

Figure 14

Matsue et al.

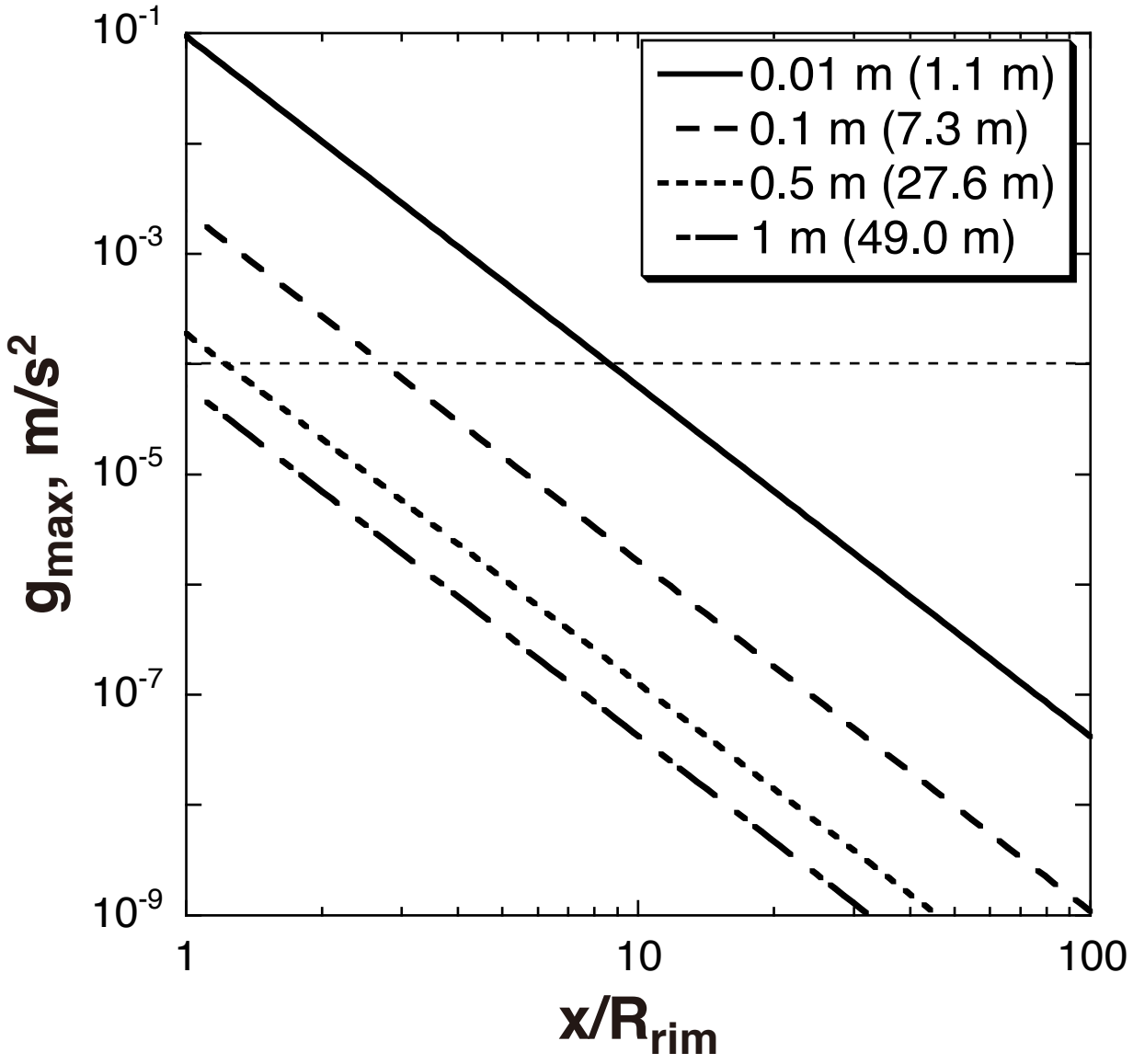

Figure 15

Matsue et al.